Heat capacity, isothermal compressibility, isosteric heat of adsorption and thermal expansion of water confined in C-S-H

Tulio Honorio, Fatima Masara, Farid Benboudjema

▶ To cite this version:

Tulio Honorio, Fatima Masara, Farid Benboudjema. Heat capacity, isothermal compressibility, isosteric heat of adsorption and thermal expansion of water confined in C-S-H. Cement, 2021, pp.100015. ⟨10.1016/j.cement.2021.100015⟩. ⟨hal-03364762⟩

HAL Id: hal-03364762

https://hal.science/hal-03364762v1

Submitted on 16 Oct 2023

Heat capacity, isothermal compressibility, isosteric heat of adsorption and thermal expansion of water confined in C-S-H

Tulio Honorio[a,*], Fatima Masara[a], Farid Benboudjema[a]

[a] *Université Paris-Saclay, ENS Paris-Saclay, CNRS, LMT - Laboratoire de Mécanique et Technologie, 91190, Gif-sur-Yvette, France*

Abstract

Nanoconfinement is known to affect the property of fluids. The changes in some thermo-mechanical properties of water confined in C-S-H are still to be quantified. Here, we perform molecular simulations to obtain the adsorption isotherms in C-S-H as a function of the pore size (spanning interlayer up to large gel pores). Then, fluctuations formula in the grand canonical ensemble are used to compute the isothermal compressibility (and its reciprocal, the bulk modulus), the heat capacity, the coefficient of thermal expansion and thermal pressure, and the isosteric heat of adsorption of confined water as a function of the (nano)pore size. All these properties exhibit a pore size dependence, retrieving the bulk values for basal spacing above 2 nm. To understand why property changes with confinement, we compute structural descriptors including the radial distribution function, apparent density, hydrogen bonds counting, and excess pair entropy of water as a function of the confinement. These descriptors reveal significant structural changes in confined water. The heat capacity shows a good linear correlation with the apparent density, entropy, and hydrogen bond number. The values of water property as a function of the basal spacing are a valuable input for multiscale modeling of cement-based materials.

Keywords: Thermal properties; Sorption; Enthalpy of adsorption;

---

[*] Corresponding author
Email address: `tulio.honorio-de-faria@ens-paris-saclay.fr` (Tulio Honorio)

Preprint submitted to Cement *October 1, 2021*

Multistability; Grand Canonical Monte Carlo.

1. Introduction

Water confined in micro- and meso-pores exhibits unique properties that may strongly differ from that of bulk water. Hydrodynamics [1], self-diffusion [2] and dielectric properties [3, 4], heat capacity [5, 6], Biot coefficient [7], phase transitions [8] and water dissociation [9] are known to be affected by water confinement in various nanoporous materials, including C-S-H. A fundamental understanding of how confinement affects the properties of fluids is crucial to elucidate the nanoscale phenomena at the origin of the behavior of materials with hierarchical porosity such as cement-based materials.

Quantifying the effects of confinement in fluids represents a significant challenge considering the length and time scales that are needed to be probed. In this context, molecular simulations are particularly well-suited to assess the behavior of confined fluids since they enable the quantification of inter-atomic forces, structural changes, and other nanoscale processes responsible for the anomalous behavior of confined fluids. Several works have tackled the question of what are the particularities of the behavior of water confined in C-S-H using molecular simulations (e.g. [10] for a review), but there are still important open questions as discussed herein.

In the case of the heat capacity of confined water, conflicting information are found in the literature. On the one hand, Bentz [11] posits that confined water would exhibit an ice-like heat capacity due to more constraints to the dynamics of hydrogen bonds in confined geometries. In agreement with this postulate, molecular simulations on C-S-H for systems in the equilibrium basal spacing (i.e the most prevalent one) shows that the heat capacity of confined water is a fraction of that of bulk water [12]. In the same study, it was also observed a decrease in the heat capacity at constant pressure with increasing water density when various C-S-H models with different Ca/Si ratios were considered. Direct simulations in which H-bonds statistics are computed for systems according to various basal spacings (not only the equilibrium basal spacing) may shed light on the pore-size dependence of the heat capacity of confined water.

On the other hand, evidence from experimental and modeling studies on other microporous materials including swelling clays [13], silica [14, 5], ion-exchange resins [15], and hydroxyapatite [6], shows that confined water may exhibit a heat capacity larger than that of bulk water. In the case of microporous silica, experiments show that the heat capacity of confined water peaks for pore sizes of about 7 nm, with a value approximately 25% larger than that f bulk water [14, 5]. An explanation for a heat capacity of confined water larger than that of bulk water is the coexistence of two populations of water, each population associated with an specific average enthalpy [16]. One population exhibits ice-like behavior (with a larger number of H-bonds [17]), while the other is associated with a large heat capacity [16]. These results show a much more complex picture required to understand the heat capacity of confined water than the one proposed so far for C-S-H based solely on a qualitative analysis of H-bonds constrains under confinement [11].

To date, no direct attempt to directly measure elastic properties (including the bulk modulus or its reciprocal, the isothermal compressibility) of confined water in C-S-H has been proposed in the literature. Evidence from shear simulations suggests that contrarily to what is observed in bulk water, confined water in C-S-H may present non-zero shear strength, corroborating the picture of glassy or solid-like behavior for confined water [18]. Studies on other phyllosilicates show that the isothermal compressibility increases with the water content N_w in swelling clays as $\propto \exp(-1/N_w)$ [19], which is consistent with the picture that confined water (or at least a fraction of confined water) would exhibit a solid-like behavior with larger stiffness than bulk water.

The isosteric heat of adsorption of water in C-S-H has been computed using molecular simulations as a function of the relative humidity for two pore sizes representative of interlayer (equilibrium basal space) and gel pores [20]. The isosteric heat of adsorption was shown to decrease with the water content in agreement with experiments [20]. More research is needed to understand how confinement affects this property in a larger range of pore sizes and under controlled RH.

Finally, confinement has been evoked as a critical aspect that explains the thermal pressurization in nanolayered adsorbing materials [21, 22]. Thermal expansion and thermal pressure coefficients are properties directly associated with thermal pressurization. Comparing to other phyllosilicates, the coefficient of thermal expansion of water is reported to decrease with increasing water content in swelling clays [19]. The coefficient of thermal expansion of C-S-H has been successfully computed using molecular dynamics for equilibrium pore sizes as a function of the Ca/Si[12]. The specific contribution of confined water in this thermal expansion and how the aforementioned properties evolve with pore size in C-S-H remain open questions.

In this work, we perform molecular simulations to obtain the adsorption isotherms in (liquid) water saturated C-S-H as a function of the pore size, spanning interlayer up to large gel pores. A realistic C-S-H model [23] is studied using hybrid Grand Canonical Monte Carlo (GCMC)/ Molecular Dynamics (MD) simulations. From the well-suited fluctuation formula, we compute the bulk modulus (and its reciprocal the isothermal compressibility), the heat capacity (at constant volume and pressure), the coefficient of thermal expansion and thermal pressure, and the isosteric heat of adsorption of confined water as a function of the (nano)pore size. The results obtained constitute valuable input for multiscale modeling and may provide new physical insights into the origins of the thermomechanical behavior of cement-based materials.

2. Molecular models and methods

2.1. C-S-H atomistic model

The C-S-H model proposed by Kunhi et al. [23], with molecular formula $C_{1.67}SiO_{3.7}$. nH_2O, is adopted. The calcium to silicon ratio Ca/Si of 1.67 is a common value measured in C-S-H obtained from Portland cement hydration [24, 25, 26]. Compared to other C-S-H models in the literature, in the present model two features related to defective crystalline structures are included: substitution of bridging silicate tetrahedron with calcium and silicate dimer with hydroxyl groups, which leads to a structure where the concentration of protonated silanol groups, as well as the mean chain length, are more consistent with experimental evidence [24].

2.2. Force field

The interactions among atoms in C-S-H structure are described based on ClayFF [27] and SPC/E water model [28]. With these force fields, the potential energy writes:

$$U^{Tot} = U^{LJ} + U^{Coul} + U^{Bond} + U^{Angle} \tag{1}$$

Short-range repulsion and van der Waals attraction are modeled with the Lennard-Jones (LJ) potential:

$$U^{LJ} = 4 \sum_{i \neq j, ij \text{ nonbonded}} \epsilon_{ij}^{LJ} \left[\left(\frac{\sigma_{ij}^{LJ}}{r_{ij}} \right)^{12} - \left(\frac{\sigma_{ij}^{LJ}}{r_{ij}} \right)^{6} \right] \tag{2}$$

where r_{ij} is the distance between particle i and j.

Electrostatic interactions are modeled with the Coulomb potential

$$U^{Coul} = \frac{e^2}{4\pi\epsilon_0} \sum_{i \neq j, ij \text{ nonbonded}} \frac{q_i q_j}{r_{ij}} \tag{3}$$

where e is the elementary charge, and $\epsilon_0 = 8.85419 \times 10^{-12}$ F/m is the dielectric permittivity of vacuum.

Lennard-Jones parameters (ϵ_{ij}^{LJ} and σ_{ij}^{LJ}) and partial charges q_i are given in Table 1. Lorentz-Berthelot mixing rule is used to compute LJ interaction involving dissimilar elements.

Bond interactions are defined only for water and hydroxide. Bond and angle interactions are described using harmonic potentials, respectively, by

$$U^{Bond}(r_{ij}) = \sum_{ij \text{ bonded}} k_B \left(r_{ij} - r_0 \right)^2 \quad \text{and} \tag{4}$$

$$U^{Angle}(\theta_{ijk}) = \sum_{ijk\,\mathrm{bonded}} k_A \left(\theta_{ijk} - \theta_0\right)^2 \tag{5}$$

The associated bond k_B and angle k_A rigidities, as well as equilibrium distance and angles, are listed Table 2. We model hydroxide based on SPC/E model. The bond length of hydroxide adopted is smaller than the original SPC/E value to better capture structural features in C-S-H as reported in ref. [23].

Table 1: Non-bond parameters and partial charges.

Species and Symbol	partial charge [e]	ϵ^{LJ} [kJ/mol]	σ^{LJ} [Å]
water hydrogen, H_w	0.4238	-	-
water oxygen, O_w	-0.8476	0.650	3.166
hydroxyl hydrogen, H_H	0.425	-	-
hydroxyl oxygen, O_H	-0.95	0.650	3.166
oxygen, O	-1.105	0.650	3.15
silicon (tetr.), Si	2.1	7.701×10^{-6}	3.302
calcium (intra), Ca	1.05	2.104×10^{-5}	5.567
calcium (inter), Ca_W	2.00	2.104×10^{-5}	2.872

Table 2: Bond parameters (for SPC/E water and hydroxide).

	k_B [kJ.mol^{-1}.Å^{-2}]	r_0 [Å]
O_w-H_w	2318.500	1.0
O_H-H_H	2318.500	0.954
	k_A [kJ.mol^{-1}.rad^{-2}]	θ_0 [°]
H_w -O_w-H_w	191.50	109.47

2.3. Molecular simulations

Hybrid GCMC-NVT simulations were carried out to sample the Grand canonical ensemble (μVT) for the fluid while keeping the number of solid particles, calcium counterions, and hydroxide constant. The imposed volume refers to a given basal spacing (directly related to the interlayer pore thickness), the dimensions along with pore plane directions remain unchanged (as generally assumed in GCMC simulation of layered adsorbing materials [29, 30]). In the hybrid simulation protocol, the GCMC stage enables the exchange of water molecules with an infinite water reservoir at imposed temperature and chemical potential (corresponding to an RH of 100%). The NVT stage allows a gain in the efficiency of the simulation by better sampling the phase space. A timestep of 1 fs is adopted. Nosé-Hoover thermostat and barostat with damping parameters of 100 and 1000 timesteps, respectively, were adopted. The particles in the C-S-H solid layer (i.e. Si, O, and Ca) are not time-integrated (i.e are not accounted for in the MD moves) to gain in computation efficiency. After the c-length was increased, a first GCMC stage with 1 million Monte Carlo (MC) moves was performed with a partial pressure exceeding 10 fold the saturating pressure in order to fill the interlayer space with water. Then, at the RH of 100%, we performed various cycles of 1 million MC to check the equilibration time: 5 cycles were sufficient to equilibrate all systems considered in this study. The production time for the c-lengths up to 6 nm were 10 million MC steps, and 6 million MC for the larger systems. Under the production stage, the system exhibits stable total energy with a coefficient of variation below 0.05% and a stable number of water molecules with a coefficient of variation below 0.50%. Ewald summation (with desired relative error in forces of 10^{-5}) is adopted to deal with long-range electrostatic interactions. Periodic boundary conditions were adopted in all directions.

The original atomic structure of Kunhi et al. [23] is orthogonal and composed of two layers, with a micro- and a meso-pore. The reported interlayer distance is 13.76 Å. Here, to obtain the initial configuration with two micropores, we have deleted all the water molecules and set the length in c-direction as 27.52 Å. Water molecules were then inserted using the GCMC-NVT simulations. Figure 1 shows a snapshot of the C-S-H structure at equilibrium basal spacing.

For further comparison, we also performed GCMC simulations on bulk (SPC/E) water using simulation boxes of 8000 nm^3 to compute the properties of the fluid using the same procedure described in Section 2.5.

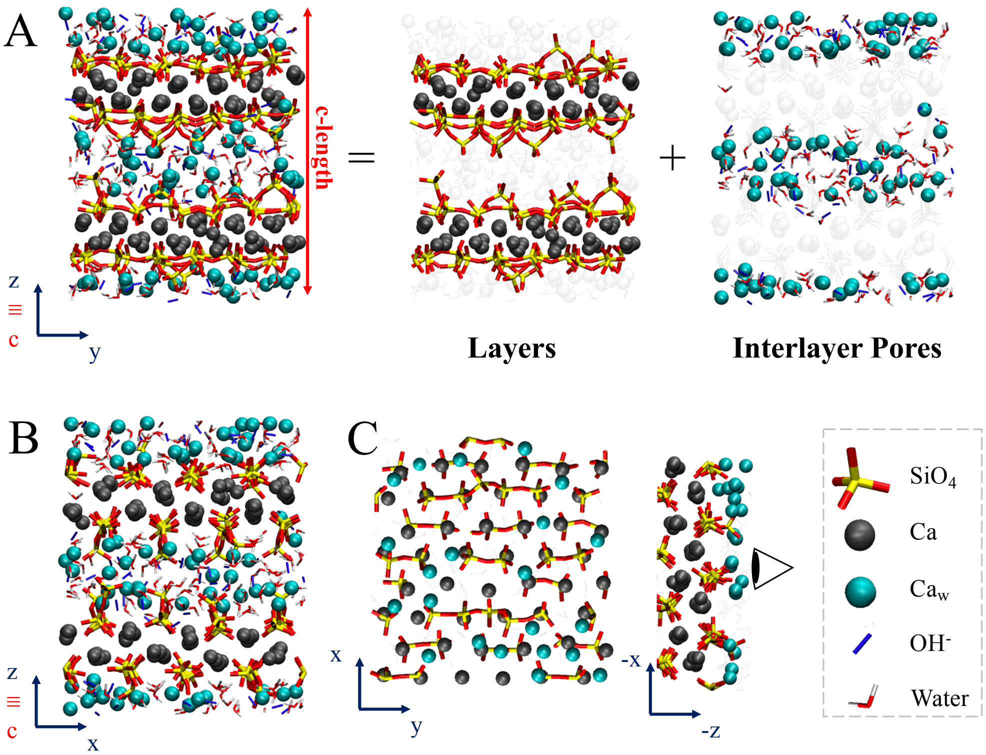

Figure 1: Snapshot of the C-S-H atomic structure at the equilibrium basal spacing d_{min} (minimum at the free energy potential). Projections according to (A) xz, (B) yz and (C) xy planes.

2.4. Stability analysis under sorption: stable basal spacings, and effective interactions

In order to simulate drained experimental conditions, the hybrid ensemble $N_s\mu VT$ based on grand canonical ensemble has been used. In this ensemble, (nano-)confined water in C-S-H interlayer pores is in equilibrium with an external water reservoir. The chemical potential of water μ, the volume V, and the temperature T are held constant. The system maintains a constant number of calcium counterions, hydroxide ions, and C-S-H solid particles N_s while only the number of water molecules is allowed to fluctuate.

The thermodynamic potential of the given system involves a function of the Helmholtz free energy F and is given as [29]:

$$\Lambda(N_s, V, \mu, T) = F - \mu N_w \tag{6}$$

where N_w is the number of water molecules. The confining pressure P is based on the thermodynamic potential Λ and is calculated using [29, 31]:

$$P = \frac{1}{S_s} \left| \frac{\partial \Lambda}{\partial d} \right|_{\mu,T} \tag{7}$$

where d is the basal spacing, and S_s is the layer surface area. The analysis of pressure isotherms enables the identification of unstable and stable zones. The mechanical stability condition imposes that whenever the pressure increase with the volume $\partial P/\partial V > 0$ the system is under an unstable equilibrium. In the case of layered materials, this condition can be written as a function of the basal spacing $\partial P/\partial d > 0$, since only dimensional changes in the basal spacing d are expected while the surface area is kept constant. Using the same argument, the expression of the energy of the system can be calculated as a function of the basal spacing d using [29, 31]:

$$\lambda = \frac{\Lambda}{S_s} = \lambda_0(d_0, T, \mu) - \int_{d_0}^{d} P d(d) \tag{8}$$

where d_0 is the reference basal spacing. The free energy Λ informs on the effective interaction, or potential or mean force (PMF), between two layers in a face-to-face configuration.

From the energy profile, one may determine the most stable configuration corresponding to equilibrium basal spacing. Basal spacing at which a free energy minimum (local or global) occurs is said to be stable. Following a stable path, the transition between stable states is only possible if the system acquires enough energy to overcome the activation barrier. If the energy barrier is on the order or smaller than the energy associated with the thermal fluctuations (i.e on the order of kT, where k is the Boltzmann constant), the transition between stable states is expected to occur due to these fluctuations. Otherwise, the system is prone to metastability.

2.5. Properties computed from molecular simulations in grand canonical ensemble

2.5.1. Isothermal compressibility (and bulk modulus), heat capacity and coefficient of thermal expansion

The fluctuation $\langle \delta\mathcal{A}\delta\mathcal{B}\rangle_{ENS}$ of two random variables is defined as the covariance: $\langle \delta\mathcal{A}\delta\mathcal{B}\rangle_{ENS} = \langle \mathcal{A}\mathcal{B}\rangle_{ENS} - \langle \mathcal{A}\rangle_{ENS}\langle \mathcal{B}\rangle_{ENS}$ for averages $\langle . \rangle_{ENS}$ on the statistical ensemble ENS to be defined. For the case of a variance of a given random variable $\langle \delta\mathcal{A}\delta\mathcal{A}\rangle_{ENS} = \langle \delta\mathcal{A}^2\rangle_{ENS}$. The properties of the adsorbate fluid can be computed in a grand canonical simulation from the fluctuations of the potential energy and number of particles [32].

The isothermal compressibility β_T (reciprocal of the bulk modulus $K = 1/\beta_T$) is given by [32]:

$$\beta_T = \frac{\langle \delta N^2\rangle_{\mu VT} V}{\langle N\rangle_{\mu VT}^2 kT} \tag{9}$$

where $\langle . \rangle_{\mu VT}$ denotes an average in the grand canonical ensemble.

The heat capacity at constant volume C_V is given by [33, 34]:

$$C_V = \frac{1}{MkT^2}\left(\langle \delta E_T^2\rangle_{\mu VT} - \frac{\langle \delta E_T \delta N\rangle_{\mu VT}^2}{\langle \delta N^2\rangle_{\mu VT}}\right) \tag{10}$$

where E_T is the internal energy, and M is the mass. In the derivation of this expression, no *a priori* assumption is made regarding the total number of degrees of freedom per molecule (for comparison, the expression in ref. [32] assumes no rotational degrees of freedom). Thus, the expression can be applied to molecules that present rotational degrees of freedom as is the case of water.

The coefficient of thermal expansion α is given by [32]:

$$\alpha = \frac{\langle P\rangle_{\mu VT}\beta_T}{T} - \frac{\langle \delta U \delta N\rangle_{\mu VT}}{\langle N\rangle_{\mu VT} kT^2} + \frac{\langle U\rangle_{\mu VT}\langle \delta N^2\rangle_{\mu VT}}{\langle N\rangle_{\mu VT}^2 kT^2} \tag{11}$$

which can also be written in an anisotropic frame as:

$$\alpha_{ij} = \frac{\langle P_{ij}\rangle_{\mu VT}\beta_T}{T} - \frac{\langle \delta U \delta N\rangle_{\mu VT}}{\langle N\rangle_{\mu VT} kT^2} + \frac{\langle U\rangle_{\mu VT}\langle \delta N^2\rangle_{\mu VT}}{\langle N\rangle^2_{\mu VT} kT^2} \tag{12}$$

where $P_{ij} = \sum_k^N \frac{m_k v_{k_I} v_{k_J}}{V} + \sum_k^{N'} \frac{r_{k_I} f_{k_J}}{V}$ is the pressure tensor computed by the virial formula, where N and N' is the total number of atoms in the system, with N' including also periodic image replicas; m_k is the mass of the particle k; v_{k_I}, r_{k_I} and f_{k_I} are, respectively, the velocity of, the position of and the force on particle k according to the direction $I(=x, y, z)$.

2.5.2. Isosteric heat of adsorption

The isosteric heat of adsorption q_{st} is a thermodynamic observable quantifying the enthalpy change associated with the adsorption of a molecule on a given surface. This quantity is key information to understand how sorption isotherms are affected by the temperature, being, therefore, a fundamental input in the modeling of drying processes in cement-based materials (e.g. [35]).

The isosteric heat of adsorption is the sum of the average energy of adsorption $q = \frac{\Delta\langle U\rangle}{\Delta\langle N\rangle}$ (i.e. the variation in the average energy $\Delta\langle U\rangle$ between two systems under the same conditions with respect to the variation $\Delta\langle N\rangle$ of the number of particles) and the energy required to push the sorbate in the bulk phase when it desorbs [36]:

$$q_{st} = -q + RT \tag{13}$$

where R is the gas constant.

In a molecular simulation, a direct evaluation of q can be made by approximation $q \approx \frac{\partial\langle U\rangle}{\partial\langle N\rangle}$, thus

$$q_{st} = -\frac{\partial\langle U\rangle}{\partial\langle N\rangle} + RT \tag{14}$$

Noise in simulation results can make it difficult to compute this derivative with precision.

Another strategy is to consider the derivative product obtained by chain rule $q \approx \frac{\partial \langle U \rangle}{\partial \langle N \rangle} = \frac{\partial \langle U \rangle}{\partial \langle \mu / T \rangle} \frac{\partial \langle \mu / T \rangle}{\partial \langle N \rangle}$. Statistical physics shows that the second derivative is $\frac{\partial \langle N \rangle}{\partial \langle \mu / T \rangle} = \langle N^2 \rangle - \langle N \rangle^2 = \langle \delta N^2 \rangle$, i.e. the variance of the number of sorbate molecules [32]. The first derivative can be also obtained from the theory as $\frac{\partial \langle U \rangle}{\partial \langle \mu / T \rangle} = -\frac{\partial \langle N \rangle}{\partial \langle 1 / T \rangle} = \langle UN \rangle - \langle U \rangle \langle N \rangle = \langle \delta U \delta N \rangle$, i.e. the cross-variance of the energy and the number of particles [36]. Finally, a fluctuation formula can be then obtained for q and the isosteric heat of adsorption reads [36]:

$$q_{st} = -\frac{\langle \delta U \delta N \rangle}{\langle \delta N^2 \rangle} + RT \tag{15}$$

as a function of quantifies that can be easily computed in GCMC simulations.

A direct evaluation of q_{st} using Eq. 13 is reported by Bonnaud et al. [20] for C-S-H with two pore sizes. In this work, we compute the isosteric heat of adsorption using the fluctuation formula (Eq. 15) for various slit pore sizes.

3. Results

3.1. Isotherms, disjoining pressure and effective interactions

Figure 2(A) displays the adsorption isotherm as a function of the c-length imposed in the GCMC-NVT simulations. The overall trend is a linear increase of the water content with the pore size following the linear fit :

$$N_w/Si\ [mol/mol] = 0.1517||c|| - 2.520 \tag{16}$$

where $||c||$ is the c-length. A zoom in the small c portion (Figure 2(B)) shows the tendency of plateau forming, which is an indication of molecule layering in the small pores (i.e. slit pore with thickness size of a few molecules diameters). In layered materials, each plateau can be associated with a stable basal spacing [29].

The disjoining or confining pressure isotherm is shown in Figure 2(C). The disjoining pressure $\Pi = P - P_c$ is defined as the difference between the confining pressure and the capillary pressure P_c. Note that for a zero capillary pressure in a liquid saturated porous media, the confining pressure is equivalent to the disjoining pressure. The pressure isotherms show an oscillatory allure at small c-lengths Figure 2(D), which is also an indication of molecule layering with each oscillation being associated with a stable basal spacing [29]. The mechanical stability condition imposes that whenever the pressure increase with the volume (or the basal spacing in the case of layered materials) the equilibrium is unstable. Unstable zones can be therefore identified in the domain of c-length 26.0-26.7 and 28.1-29.2 Å (gray rectangles in Figure 2(D)).

We also compute the partial contribution of each electrolyte species and solid layer to the disjoining pressure. As observed in previous studies [37], the calcium counterions exhibit the most negative pressure contributing to the cohesion of the material. As in the (total) pressure curve, all partial pressures go to zero with the increase in the pore size. The partial pressures also show an oscillating pace at small c-lengths Figure 2(D).

Figure 3 shows the effective interactions of the layers in a face-to-face configuration. The minimum of the potential appears at d_{min} of 13.7 Å, which is, therefore, the most prevalent basal spacings in a system under equilibrium under pressure control. Thus, the basal spacing can be related the c-length in our results using the expression (in Å):

$$d = ||c|| - 13.7 \tag{17}$$

We also identify other possible equilibrium hydration states: $d_{0W?}$=11.8 Å and $d_{2W?}$18.3 Å. We added the "?" to indicate that our simulation results do not enable to identify with certainty that these points are associated with local minima due to a lack of resolution in terms of c-length for $d_{0W?}$ or lack of precision in pressure computation for $d_{2W?}$. For the latter, the potential well depth is on the order of the simulation precision. Note that other simulation protocols than GCMC simulation may be necessary to sample with precision basal spacings associated with higher hydration states [38].

The potential well depth is approximately $20kT/\text{nm}^2$, which is one order of

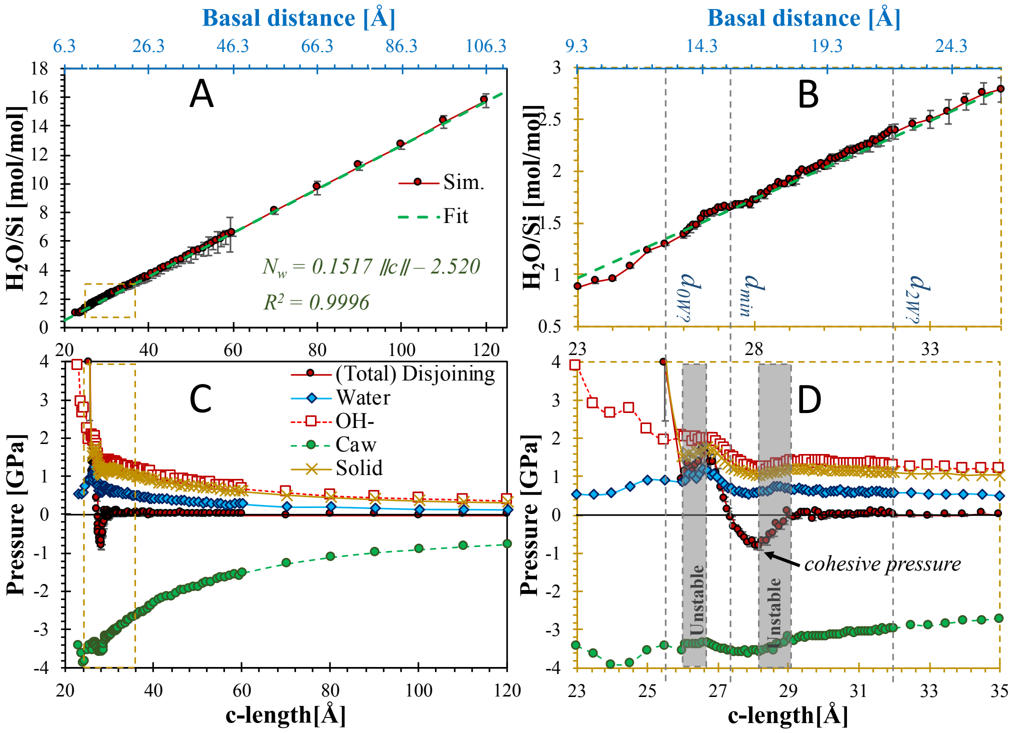

Figure 2: (A) Adsorption isotherm and respective zoom (B) in the small c-length portion (B). (C) Disjoining pressure, and confining pressure per electrolyte species (water, hydroxide, and calcium counterion) and in the solid layer, and respective zoom (D) in the small c-length portion. In both cases, the dashed yellow rectangles show the portion zoomed in. A linear fit of adsorption isotherm is shown. In (D), the domain of unstable equilibrium ($\partial P/\partial d > 0$) is identified with the gray rectangles.

magnitude smaller than the value computed for tobermorite [30] but remains larger than the values observed in swelling clays [29] (the hydrophilicity of the pore walls are known to change the structure of vicinal water [8] and counterions correlations might also play an important role in the effective interactions of layered materials). To analyze the susceptibility of a system to metastability, the potential well depth can be compared with the energy associated with thermal fluctuations, which is on the order of kT. An energy barrier much larger than

kT means that thermal fluctuations are generally not sufficient for the system to overcome a transition to another hydration state. Therefore, the studied system is prone to metastabilities.

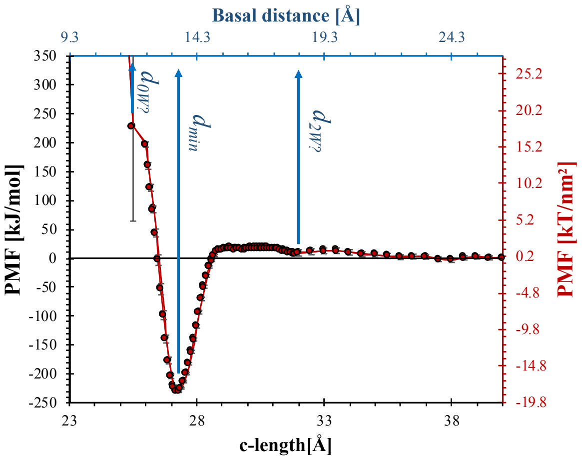

Figure 3: Potential of mean force (PMF) as a function of the c-length and basal spacing (which here are related through the expression in Eq. 17). The equilibrium basal spacings are displayed.

Table 3 gathers the parameters and properties that can be inferred from the pressure isotherms and effective interaction in a comparison with data from the literature. The cohesive pressure $P_{co} = minP(d)$ is the pressure needed to disjoin two solid layers (i.e. it corresponds to the global minimum in the pressure isotherms). The out-of-plane elastic modulus E_{zz} can be computed from slope in the pressure isotherms at a given basal spacing d_i: $E_{zz} = -d_i \left.\frac{\partial P}{\partial d}\right|_{d_i}$, where we have choose $d_i = d_{min}$. The surface energy γ_s is the work needed to put two layers apart: $\gamma_s = -\frac{1}{2}\int_{d_{min}}^{\infty} Pd(d)$. The values of basal distances and E_{zz} are within the range of variability of the data from the literature. The cohesion pressure obtained here is closer to the experimental values reported by Plassard et al. [39] and the simulation of Bonnaud et al. [40] also in a disordered C-S-H. Other simulations studies in the literature [41, 4, 30, 42] report a P_{co} a few gigapascals larger than the value obtained here, with studies on tobermorite

[41, 30, 42] reporting the larger cohesive pressures.

Table 3: Equilibrium stable basal (d_1, d_2, d_3) spacing, cohesive pressure P_{co}, surface energy γ_s and out-of-plane Young modulus E_{zz} (computed only for the d_{min}): comparison with experimental and simulation data from the literature.

d_1 (d_2) [d_3] [Å]	P_{co} [GPa]	γ_s [J/m^2]	E_{zz} [GPa]	Ref.
12.7? 13.7 (16.0?)	0.82	0.10	67.4	This work
	-	0.32-0.4	-	[43, 44] *
-	0.93	-	-	[39] *
12.5 (14.3) [16.1]	5.0	-	-	[41]
-	-	-	61, 89	[45, 46] *
11.4	0.931	-	42.28	[40]
10.4 (13.0) [15.7]	3.7	0.1716	102.43	Ca/Si=1.5 [4]
10.4 (12.9) [15.5]	3.0	0.1905	81.74	Ca/Si=1.7 [4]
12.6 (15.7)	4.17	0.61	61.5	[30] **
13.5 (15.9)	6.5	0.67	77.6	[42] **

*Experimental. **Tobermorite.

Water ordering adjacent to the pore walls is analyzed using z-profiles in Figure 4. As discussed in detail in ref. [30] in the case of tobermorite, here with a more disordered calcium silicate hydrate structure, we also observe the effect of roughness of the layer surface disturbing the ordering of adsorbed species. Water and calcium ions are adsorbed within the cavities formed by silica chains projected outwards the layer surface. Note that in small basal spacings, calcium counterion ordering is highly impacted with a three layer configuration appearing in c-lengths below 3 nm. For c-length above 3 nm, calcium counterions are structured in a two layer configuration adjacent to each pore wall with the second layer density decreasing as a function of the c-length. In all cases, hydroxides remain in-between the peaks observed for calcium counterions, which shows a strong correlation between these ions. Indeed, hydroxide ions form complexes with calcium counterions which can be associated with (micro)portlandite formation [47, 10]. However, the Caw-Oh distances obtained here, due to ClayFF parameters, are smaller than the ones reported to 1D, 2D or bulk portlandite [48].

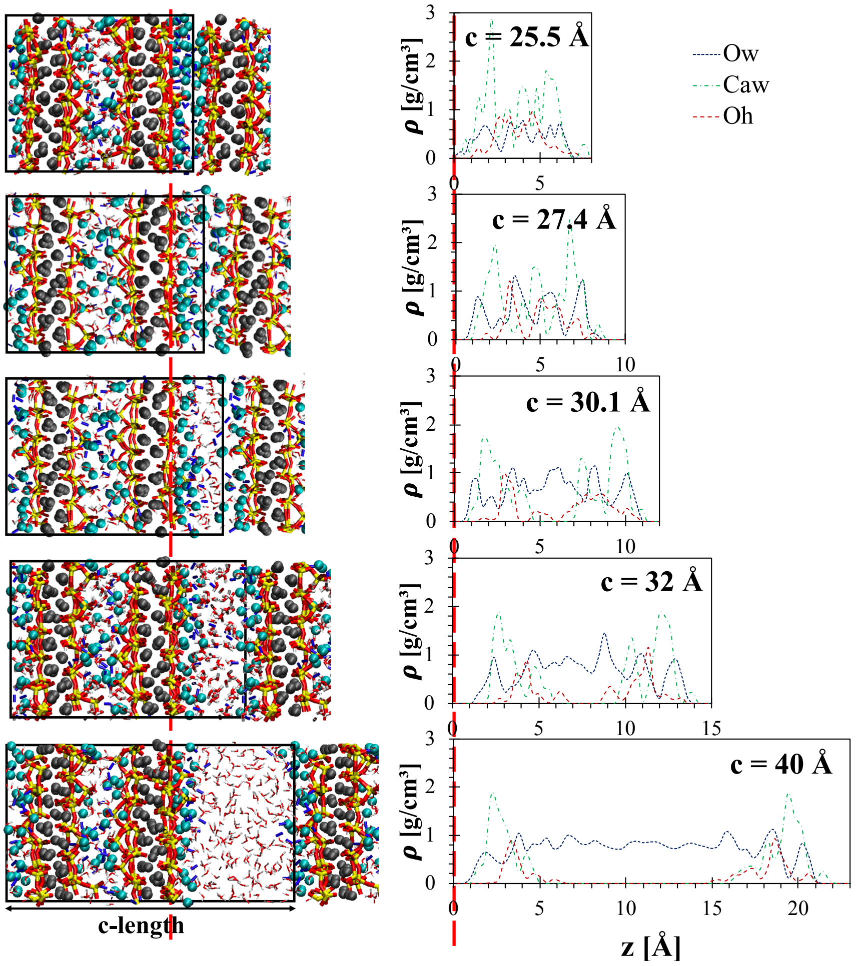

Figure 4: At left, snapshot of various pore sizes studies(from top to bottom c-length : 25.5(=$d_{0W?}$), 27.4 (=d_{min}), 30.1, 32 (=$d_{2W?}$) and 40 Å). At right, the respective density profiles (of the associated to the left pore) of water oxygen (Ow), hydroxide oxygen (Oh) and calcium counterion (Caw) as a function of the z coordinate. The vertical red line depicts the interface with z=0 imposed.

3.2. Structural data and validation of C-S-H model

In this section, the structural features and water content obtained for the stable basal spacings are compared with relevant experimental and simulation data from the literature.

Radial and pair distribution functions provide information on the structural features of ordered and disordered materials that can be used to validate atomistic models and simulations. The partial radial distribution function $g_{i-j}(r)$ (RDF) of species i and j reads (e.g. [49]):

$$g_{i-j}(r) = \frac{\rho_{i-j}(r)}{\rho_0} = \frac{1}{N_t \rho_0 x_i x_j} \sum_{k=1}^{N_i} \sum_{l \neq k}^{N_j} \delta \langle \mathbf{r} + \mathbf{r}_k - \mathbf{r}_l \rangle \tag{18}$$

where N_t is the total number of particles, ρ_0 is the number density, $x_i = N_i/N_t$ is the fraction of species i (respectively, $x_j = N_j/N_t$), and $\mathbf{r}_k$ is the position vector of particle k of species i (respectively, $\mathbf{r}_l$ is the position vector of particle l of species j).

The weighted average of the partial pair distribution function reads [50]:

$$g_w(r) = \sum_{ij} \frac{x_i x_j f_i(Q) f_j(Q) g_{i-j}(r)}{\langle f(Q) \rangle^2} \tag{19}$$

where $\langle f(Q) \rangle = \sum_i x_i f_i(Q)$, $f_i(Q)$ is assumed to be equal to the effective number of electrons Z for species i (with Z=1, 8, 14 and 20 for H, O, Si and Ca, respectively [50]).

The pair distribution function N_{i-j} can be computed from g_w by (e.g. [51, 52]):

$$N_{i-j} = 4\pi r^2 \rho_0 g_w(r) \tag{20}$$

Radial and pair distribution functions obtained from simulation (for equilibrium c-length of 27.4 Å (i.e d_{min}=13.7 Å) and experiments are compared in Figure 5. The simulated structure exhibits some of the experimental peaks also observed by Soyer-Uzun et al. [50] in C-S-H with Ca/Si of 1.6 and 1.75. A non-negligible shift is observed especially in the peak at $r \approx$1.6Å and 2.4Å.

Note that the peak at ≈ 1 Å in the simulated $N(r)$ is due to O-H pairs (we have included all pairs in the computations of $N(r)$). That peak should not show up in the X-ray data since hydrogen is almost transparent to X-ray.

We also compute the structure factor $S(Q)$ (Figure 5(B)), associated with the Fourier transform of the RDF, and compare with the experimental data from the same authors. Some of the experimental structural features, as quantified by the structure factor, are captured by the C-S-H model used here.

The radial distribution functions are compared with the non-porous calcio-silicate glass and tobermorite 14Å reported by Pellenq et al. [53]. The first peaks are similar for both Ca-O and Si-O pairs, the latter being expected due to the utilization ClayFF. The second peaks in both Ca-O and Si-O pairs obtained in our simulations exhibit features of the calcio-silicate glass, and to a lesser extent also that of the crystalline system. The small peak at $r \approx$3.2Å observed in the Ca-O RDF of tobermorite is not observed in our simulation nor the disordered system.

In figure 6, X-ray diffraction patterns obtained from simulation are compared to the experimental patterns reported by various authors [54, 55, 56, 57]. The difference between the experimental X-ray pattern XRD_{exp} and the simulated pattern XRD_{sim} is quantified using the error estimation:

$$R_{error} = \frac{|\int_{2\theta_i}^{2\theta_f} XRD_{exp} d(2\theta) - \int_{2\theta_i}^{2\theta_f} XRD_{sim} d(2\theta)|}{\int_{2\theta_i}^{2\theta_f} XRD_{exp} d(2\theta)} \tag{21}$$

where $|.|$ denotes the absolute value function, and the integration is performed in all cases from $2\theta_i = 5°$ up to $2\theta_f = 45°$ (for Martin et al. [56] tobermorite and Janik et al. [54] C-S-H) or $2\theta_f = 65°$ (for Cong et al. [55] C-S-H). The differences between simulated and experimental patterns in the appropriate 2θ ranges are $R_{error} = 5\%$ for Martin et al. [56] tobermorite, $R_{error} = 8\%$ for Janik et al. [54] C-S-H, and $R_{error} = 20\%$ for Cong et al. [55] C-S-H.

Figure 7 shows the water content and stable basal spacing obtained from simulations compared against various experimental and simulation data from the literature according to the Ca/Si ratio. The water content associated with

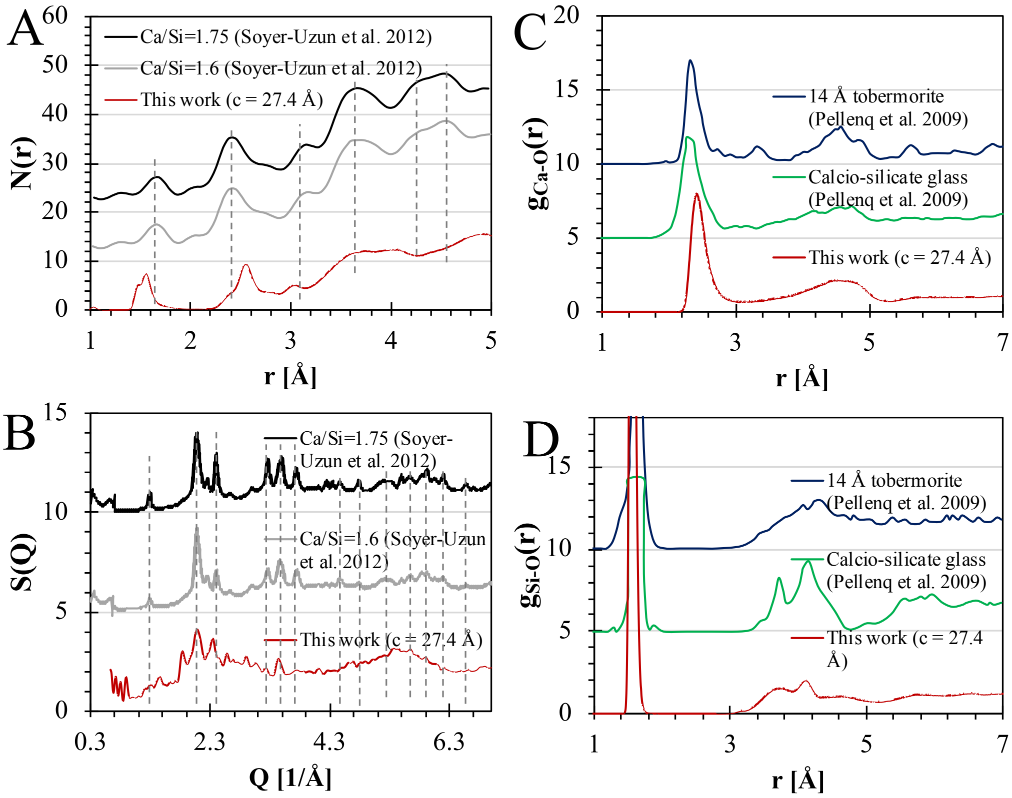

Figure 5: (A) Pair distribution function $N(r)$, and (B) structure factor $S(Q)$ compared to the experimental data of Soyer-Uzun et al. [50] for C-S-H with Ca/Si of 1.6 and 1.75. Radial distribution functions $g_{i-j}(r)$ of (C) Ca-O and (D) Si-O pairs compared to the data reported by Pellenq et al. [53] on non porous calcio-silicate glass and tobermorite 14Å.

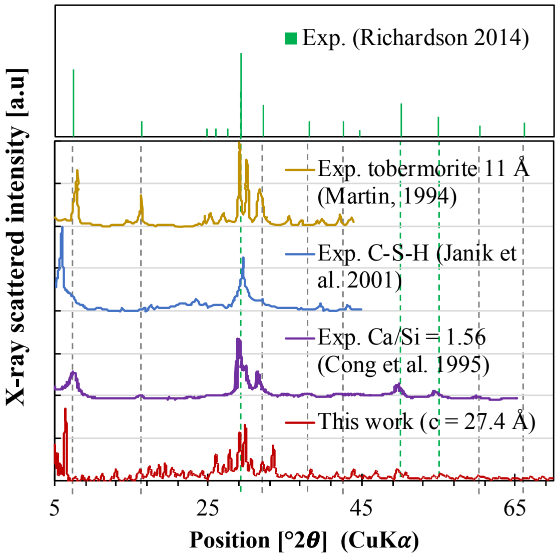

Figure 6: XRD patterns obtained from simulations at stable basal spacing c =27.4Å (using Debyer code (https://debyer.readthedocs.io)) compared against experimental data [54, 55, 56] from the literature (at the top, typical patterns of C-S-H presented by Richardson et al. [57]).

the most prevalent basal spacing d_{min} observed in simulation is consistent with the data available. The water content associated with this and the other stable basal spacings obtained from simulation are in good agreement with the three hydration states discussed by Gartner et al. [58]. According to Figure 7(B), data from the literature show that the basal spacings tend to decrease with increasing Ca/Si. The metastable $d_{0W?}$ is close to the values reported in the literature. The basal spacing d_{min} is larger than expected for a Ca/Si of 1.67. Simulations of Morshedifard et al. [59] shows that basal spacing decreases with the Ca/Si when silicates (S=SiO_2 in cement notation) are removed and increase with the Ca/Si when interlayer (micro)portlandite (CH=$Ca(OH)_2$ in cement notation) is added. This observation suggests that the large basal spacing observed here may be related to the amount of microportlandite in the interlayer in the Kunhi et al. [23] C-S-H model.

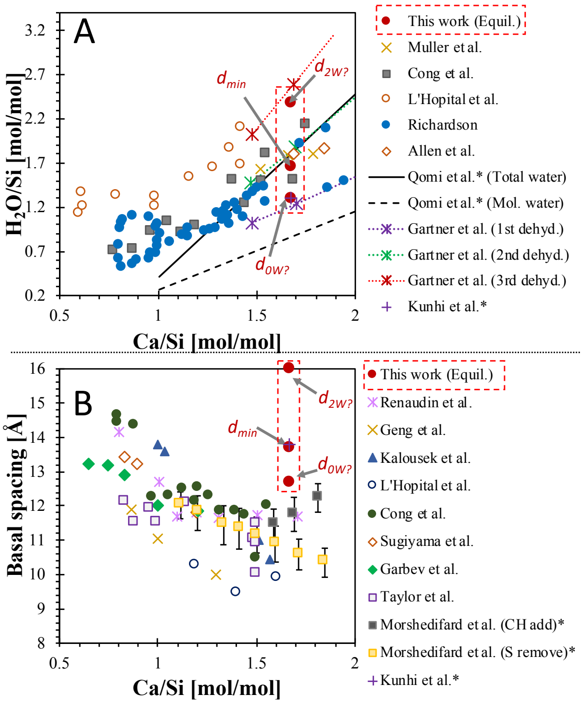

Figure 7: (A) Water content and (B) basal spacing as a function of the Ca/Si ratio: comparison with data from the literature (experimental [58, 60, 55, 57, 25, 61, 62, 63, 64, 65, 66], and simulation (marked with an "*") [67, 59, 23]). Simulations of Morshedifard et al. shows that basal spacing decreases with the Ca/Si when silicates (S=SiO_2 in cement notation) are removed and increase with the the Ca/Si when interlayer (micro)portlandite (CH=$Ca(OH)_2$ in cement notation) is added.

3.3. Dependence of the structure and thermo-mechanical properties of water on the pore size

Confinement induces changes in the water structure which may result in different physical properties. These structural changes are quantified using the radial distribution function in Figure 8. For systems with c-length as large as approximately 4-6 nm, the structure of confined water retrieves the one observe in bulk conditions. The first peak in Ow-Ow RDF (Figure 8 (A)) is slightly shifted to the left and is narrower with the confinement. Figure 8(C) shows the position of the first peak (the argument of $g_{Ow-Ow}(r)$ when it reaches its maximum) in Ow-Ow RDF as a function of the c-length. From c-lengths above 4 nm, the position of the peak is > 2.7 Å, close the values corresponding to bulk water. For smaller c-lengths, a decrease of this peak position with confinement shows that the confined water densifies with the confinement. The second peak of Ow-Ow pairs in bulk water is divided into an intermediary peak at $r \approx 3.5$ Å and another peak at $r \approx 5$ Å in systems with c-length smaller than approximately 3 nm.

The first peak in Hw-Hw RDF (Figure 8 (B)) refers to hydrogen in the same water molecule, being therefore at a distance imposed by the equilibrium bond and angle in Eq. 4) and 5. The second and the third peaks exhibit shifts to the left with the confinement; and a fourth peak (in the range 5-7 Å) is more pronounced under higher confinement. Figure 8(D) shows the position of the second peak in Hw-Hw RDF as a function of the c-length. A decrease of this peak position with confinement is also observed for c-lengths below 4 nm, which is an additional indication of densification.

To evaluate the variations in water density, we define the apparent density ρ^* as function of the volume occupied by the water V_w:

$$\rho^* = \frac{N_w m_w}{V_w} = \frac{N_w m_w}{V(N_w) - V(N_w \to 0) - \sigma_O^{LJ} S_s} \tag{22}$$

where m_w is the mass of one water molecule, $V(N_w)$ is the volume at equilibrium water content N_w, $V(N_w \to 0)$ is the extrapolation (using the expression in Figure 2(A)) of the volume at dehydrated state; and the term $\sigma_O^{LJ} S_s$ is a function of the Lennard-Jones diameter of oxygens σ_O^{LJ} (see table 2) and the xy surface area S_s of the simulation box, this terms accounts for the space that cannot be occupied by water at the interfaces due to steric repulsion. With this definition of density, we obtain ρ^* tending to the bulk density of water as the pore size increases, as shown in Figure 9. The apparent density increases significantly with the decrease in basal spacing which suggests a more compact packing of water molecules. The more compact arrangement can be associated to ordering adjacent to the hydrophilic C-S-H layers as shown in Figure 4.

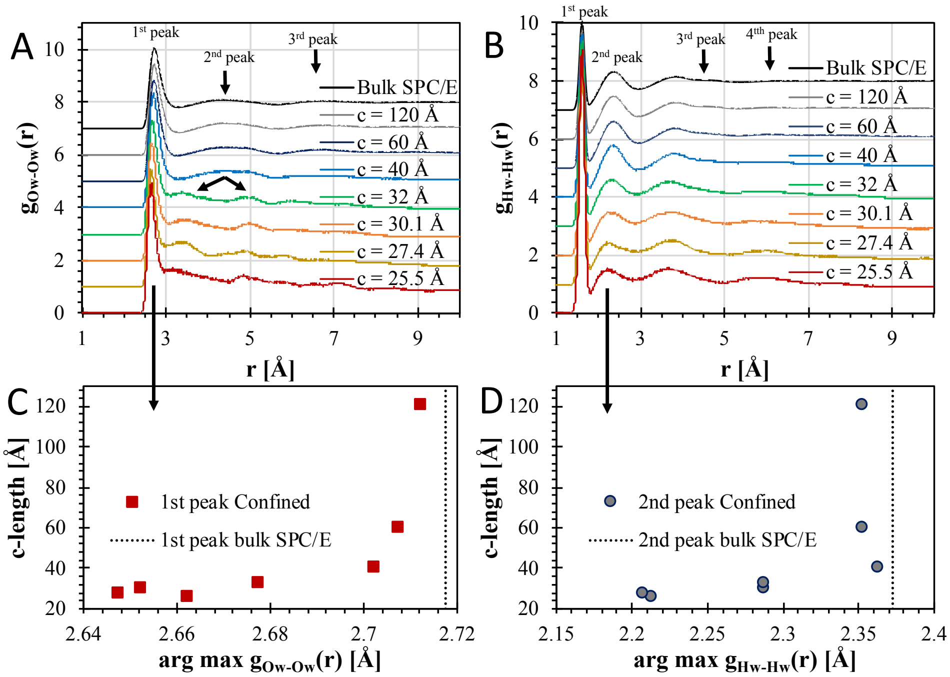

Figure 8: Radial distribution function of (A) Ow-Ow and (B) Hw-Hw pairs of water confined in C-S-H compared to bulk water. The peaks indicating the nearest, second (first peak), second, third, etc nearest correlations are labeled. The bifurcation of the second peak in Ow-Ow RDF for a c-length below 4 nm is also indicated. The positions of (C) the first peak in Ow-Ow RDF and (B) second peak in Hw-Hw RDF (the first peak is imposed by the equilibrium bond and angle in Eq. 4) and 5).

3.3.1. Bulk modulus and isothermal compressibility

Figure 10(A) and (B) shows how the bulk modulus and its reciprocal, the isothermal compressibility, of confined water change as a function of confinement. For systems with c-length as large as approximately 3 nm, confined water retrieves the bulk modulus of bulk water. In systems with smaller pores, water exhibits a larger bulk modulus than bulk water (i.e. smaller isothermal compressibility than bulk water). For c-lengths ranging from 3 to 5 nm, the isothermal compressibility of confined water is much larger than that of bulk

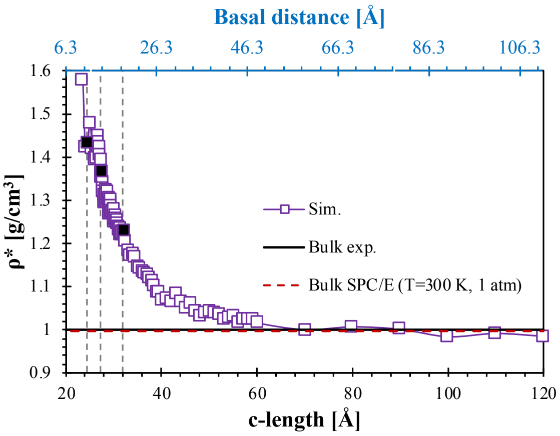

Figure 9: Apparent density ρ^* (Eq. 22) of water computed as a function of the c-length.

water, whereas the bulk modulus of confined water is only slightly smaller than the bulk value. This effect is expected since for small values of bulk modulus, as is the case here with a bulk modulus of the order of a gigapascal, the isothermal compressibility is quite sensible to any diminution of the bulk modulus (to illustrate, at the limit, when K goes to zero, β_T tends to infinity).

A lower compressibility of confined water can be associated with a more compact structure. This general trend is in agreement with the apparent density increasing significantly for small basals spacings (Figure 9) as well as with the decrease in Ow-Ow and Hw-Hw distances observed in the RDFs of water (Figure 8). However, it is more challenging to explain the larger isothermal compressibility in the 3 to 5 nm c-length range. A possible explanation could be found in the structural (or phase) transitions observed in the RDF for between c-lengths ranging from 3 to approximately 4 nm: the coexistence of phases or even the existence of a transition state with larger compressibility could explain the differences observed in the β_T as a function of the confinement in this range.

3.3.2. Coefficients of thermal expansion and thermal pressure

The coefficient of thermal expansion of water as a function of the c-length is shown in Figure 11(A). The diagonal components ($\alpha_x = \alpha_{xx}$ in Eq. 12, $\alpha_y = \alpha_{yy}$

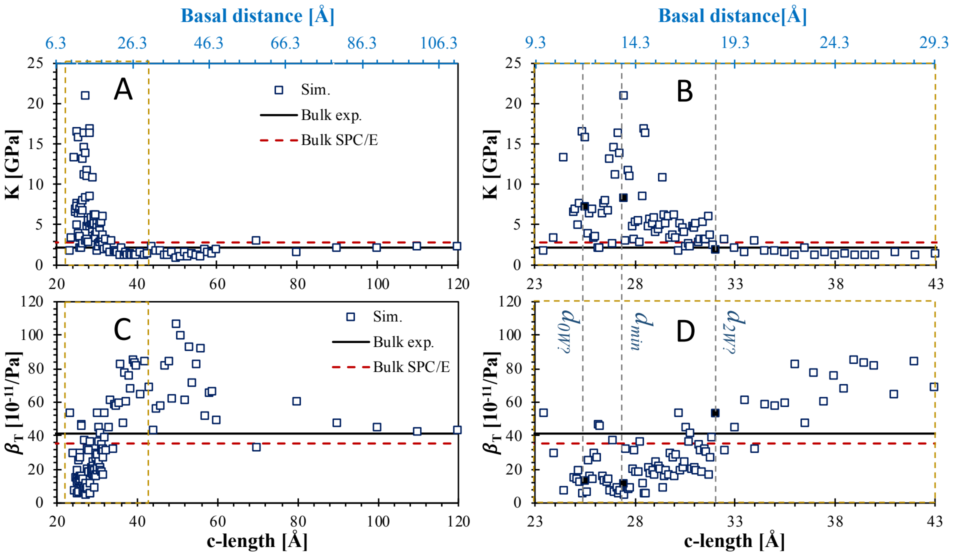

Figure 10: (A) Bulk modulus, and (C) isothermal compressibility of water confined in C-S-H as a function of of the c-length. (B) and (D) show the respective details on the 23-43 Å c-length domain. The filled symbols refers to the stable basal spacings as indicated. The experimental and SPC/E model values concerning bulk water are taken from ref. [68]

and $\alpha_z = \alpha_{zz}$) of the tensor of coefficients of thermal expansion are also shown in order to highlight the possible anisotropic response. Note that the coefficient of thermal expansion of bulk SPC/E water $\alpha_V = 51 \times 10^{-5}$ 1/K reported in the literature is almost twice the experimental value $\alpha_V = 21 - 27 \times 10^{-5}$ 1/K [69]. In contrast with this result, the $\alpha_V = 20 \times 10^{-5}$ 1/K of bulk water obtained in our GCMC simulations is closer to the experimental value. The thermal expansion of confined water is smaller than the bulk's one. This observation is in agreement with the supercooled nature of confined water since waters α_V is reported to decrease when the temperature decrease [69].

The coefficient of thermal pressure of water, defined as the products of the bulk modulus and the coefficient of thermal expansion $\gamma_V = K\alpha_V$, is displayed in Figure 11(B). The values of γ_V associated with the stable basals spacings are smaller than the values of bulk water.

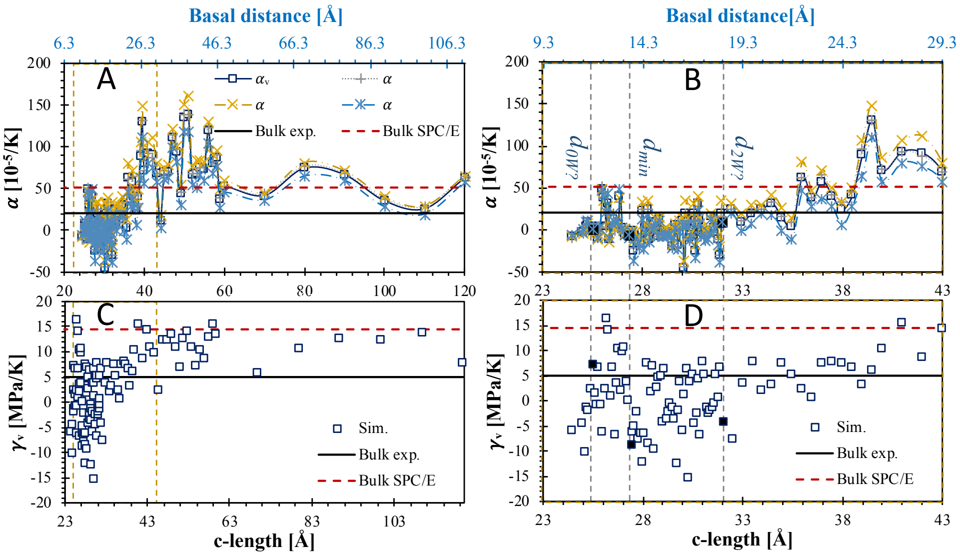

Figure 11: (A) Coefficient of thermal expansion of water as a function of the c-length. For a response which is approximately isotropic the components along each direction are expected to be close to the volumetric value (i.e. 1/3 of the trace of the tensor of coefficients of thermal expansion): $\alpha_x \approx \alpha_y \approx \alpha_z \approx \alpha_V = \frac{1}{3}(\alpha_x + \alpha_y + \alpha_z)$. The experimental and SPC/E model values of the coefficient of thermal expansion concerning bulk water are taken from ref. [69]. (C) Coefficient of thermal pressure $\gamma_V = K\alpha_V$ of water as a function of the c-length. (B) and (D) show the respective details on the 23-43 Å c-length domain. The experimental and SPC/E model values of the coefficient of thermal pressure are computed from the corresponding values of coefficient of thermal expansion (from ref. [69]) and bulk modulus (from ref. [68]).

3.3.3. Heat capacity

Figure 12 (A) and (B) shows the heat capacities at constant volume C_V and constant pressure C_P as a function of the C-S-H system c-length as obtained by GCMC simulations. The heat capacity at constant pressure C_P can be computed from C_V and the coefficient of thermal expansion and the isothermal compressibility via Mayer's relation (e.g. [70]):

$$C_P - C_V = V_w T \frac{\alpha_v^2}{\beta_T} \tag{23}$$

where the definition of the volume occupied by the water V_w as in Eq. 22 was used. The heat capacities of confined water retrieve the bulk values for c-lengths exceeding 3-4 nm. We observe heat capacities of confined water that are higher than the bulk values, in agreement with studies in other nanoporous materials [5, 17, 6]. The origin of this phenomenon has been attributed to the (co)existence of two population with specific enthalpies [5, 17]: one with supercooled or ice-like behavior (with a larger number of H-bonds [17]), another with large heat capacity [16]. Also, a high heat capacity agrees with the "supercooled picture" of water confined in C-S-H: experimental evidence shows that the heat capacity at a constant pressure of water increases markedly with decreasing temperature [71].

A heat capacity of confined water that is larger than the bulk one challenges previous simulation studies on C-S-H. Qomi et al. [12] reported an apparent heat capacity of interlayer water (in equilibrium basal spacing) as only a fraction of that of the bulk water (this result being in agreement with Bentz's postulate discussed in the introduction [11]). Qomi et al. [12] compute the heat capacity of confined water indirectly by the difference between the heat capacity of hydrated and dry (i.e. in which all interlayer water molecules are removed) systems. This approach does not take into account that in the saturated systems the presence of water changes the energetics of the solid layers and interlayer ions. In other words, the heat capacity of confined water should be not only the difference between the heat capacity of the saturated system and the heat capacity of a system without water but also take into account how the presence of water changes the potential energy of the layer and interlayer ions (i.e the difference between the energy of the dry system and the energy of the layer and interlayer ions in a hydrated system is not expected to be zero).

To shed light on the origins of these differences, we also compute the to-

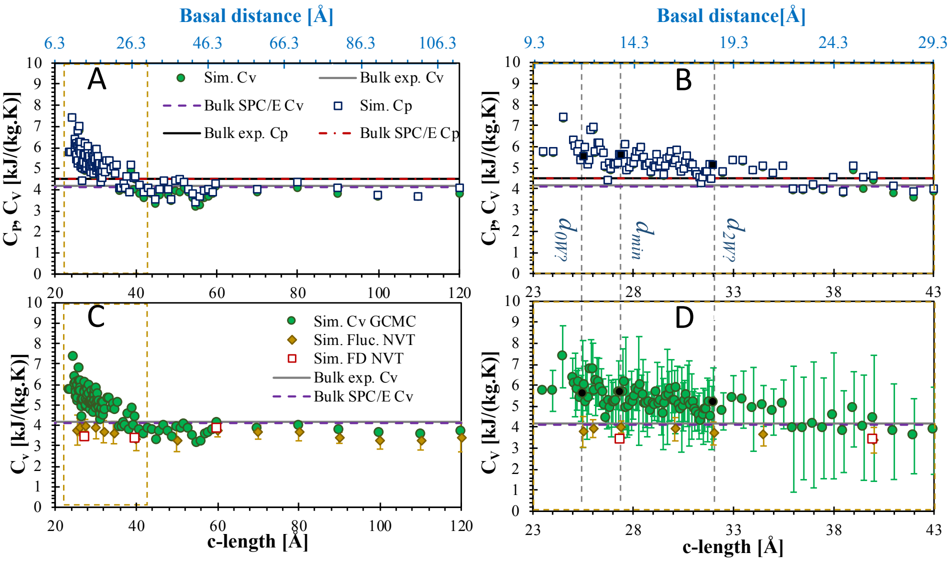

Figure 12: Heat capacity at constant volume C_V and at constant pressure C_P as a function of the c-length. In (A) the entire range of c-length is displayed; in (B), we zoom in the 23-40 Å range to highlight the values associated with the basal spacings $d_{0W?}$, d_{min} and $d_{2W?}$. The experimental and SPC/E model values of the heat capacities are taken from refs. [72] and [73], respectively. (C) Comparison of C_V of confined water computed using GCMC simulations, and NVT simulations in finite difference (FD, Eq. 24) and fluctuation (Eq. 25) approaches. In (D), we zoom in the 23-40 Å range to highlight the values associated with the basal spacings $d_{0W?}$,d_{min} and $d_{2W?}$. The standard deviations are shown for GCMC results only in (D) for the sake of readability.

tal heat capacity at constant volume of C-S-H using both a finite difference approach and fluctuation-dissipation formula in saturated systems.

For the finite difference approach, independent NVT simulations were performed for T ranging from 280 to 350 K. For the fluctuation-dissipation approach, NVT simulations at 300 K were performed for some selected c-lengths. In both cases, a timestep of 0.1 fs for a production run of 0.1 ns and Nos-Hoover thermostat with a damping parameter of 100 timesteps are adopted. The atoms in the solid layers are also time-integrated. During the production run, the total energy of the system E_T, and the total energy of water E_w were averaged, as well as their respective squares (E_T^2,E_w^2) in the case of the fluctuation-dissipation approach. In the finite difference approach we use the definition of C_V (e.g. [32]):

$$C_V = \left| \frac{\partial E_T}{\partial T} \right|_V \tag{24}$$

as the variation of the total energy E with respect to T as constant volume V. In the fluctuation-dissipation approach, C_V is computed from the fluctuation of total energy (e.g. [32]):

$$C_V = \frac{\langle \delta E_T^2 \rangle_{NVT}}{kT^2} \tag{25}$$

In both approaches, the heat capacity of water can be directly computed considering the internal energy of water E_w in the formula. Also, the heat capacity of solid layer and interlayer ions can be computed using $E_{sol} = E_T - E_w$.

Figure 13 shows the excess energy (with respect to the internal energy at 300 K) for the NVT simulations were performed for T ranging from 280 to 350 K. From Eq. 24, the slope of the curve gives the heat capacity and constant volume.

Figure 12 (C) and (D) shows the comparison of C_V of confined water computed using GCMC simulations, and NVT simulations in finite difference (FD, Eq. 24) and fluctuation (Eq. 25) approaches. Both NVT approaches are in agreement yielding a heat capacity of confined water slightly below the bulk value irrespective of the confinement. GCMC and NVT yield similar results for c-lengths above approximately 3 nm. It is unclear why the results diverge for small pore sizes.

For further comparison, the heat capacity of C-S-H (c =27.4Å) obtained from the NVT simulation is 0.81 kJ/(kg.K) (finite difference) and 0.79 kJ/(kg.K) (fluctuation). These values compare well with the results of Qomi et al. [12] which obtained C_V of C-S-H in the range 0.85-0.96 kJ/(kg.K) according to various Ca/Si ratios. The heat capacity of "dry" C-S-H in our case (i.e only the particles in the solid layers and interlayer ions) is 0.30 kJ/(kg.K) for both finite

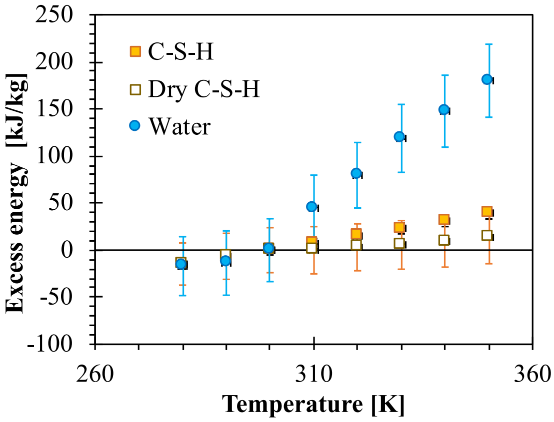

Figure 13: Excess energy with respect to the energy at T= 300 K for water saturated C-S-H (system at equilibrium basal spacing d_{min}) obtained in NVT simulations. The energy was computed for the whole system (C-S-H), water, and "dry" C-S-H (i.e only the particles in the solid layers and interlayer ions).

difference and fluctuation approaches.

One possible explanation for the differences observed between NVT and GCMC simulations could come from finite-size effects. In small systems, insertion/deletion of one water molecule affect more significantly the coefficients of variation of both the number of water molecules and the energy since there are fewer water molecules in the system. Finite size effects are recognized to affect the estimations of some properties from molecular simulation (e.g. [74, 75]). To check for finite-size effects we also run simulations with a system with twice the volume of the simulation box. With these simulations, the high values of C_V at small c-lengths were also obtained. Therefore, finite-size effects cannot explain the differences observed between NVT and GCMC estimations.

Different simulation techniques show that the heat capacities of confined water in C-S-H retrieve the bulk values for c-lengths exceeding 3-4 nm. In smaller systems, results from NVT simulation differ from results of GCMC simulations. Additional studies are required to fully understand the origins of these disparities at ultra-confined systems. Both NVT and GCMC results obtained here show a heat capacity of confined water that is either higher or only slightly smaller than the heat capacity of bulk water.

For further validation, we estimate the heat capacity of cement pastes and compare the results with the experimental data from Bentz [11] in Figure 14. A mixture rule is the right theoretical framework to upscale the heat capacity [12, 76]:

$$C_P^{est} = \sum_i f_i^m C_{P,i} \tag{26}$$

where f_i^m is the *mass* fraction of phase i, and C_P, i is the heat capacity at constant pressure of phase i. The phases present in the cement pastes and their volume fraction are estimated as a function of the w/c and degree of hydration following Knigsberger et al. [77] (see the Supporting Information for details). In this approach, the phases accounted for are capillary porosity, gel porosity, air (or chemical shrinkage), C-S-H, CH, and clinker. Also, C-S-H densification is accounted for in agreement with NMR experimental evidence [77]. Since the heat capacity of confined water retrieves the bulk value for basal distances above approximately 3 nm, both capillary and gel water heat capacity are taken as the bulk experimental value of 4.18 kJ/(K.kg) [72]. The heat capacity C_P for air and CH are 1.012 kJ/(K.kg) and 1.15 kJ/(K.kg) [78], respectively; and for solid “dry” C-S-H 0.30 kJ/(kg.K), as discussed above. We use as C_P of water confined in C-S-H the values obtained from:

- μVT simulations: C_P =5.6 kJ/(K.kg), and
- NVT simulations: C_P= 3.9 kJ/(K.kg).

Both values refer to the equilibrium basal spacing d_{min}, which must be the most prevalent basal spacing in C-S-H gel. The cases in which the μVT simulation values are used lead to estimates closer to the experimental data. But we note that the effective heat capacity of the cement paste is not strongly affected by the choice of the interlayer water C_P. This is expected since the mass fraction of water in C-S-H at the equilibrium basal spacing is only 0.155.

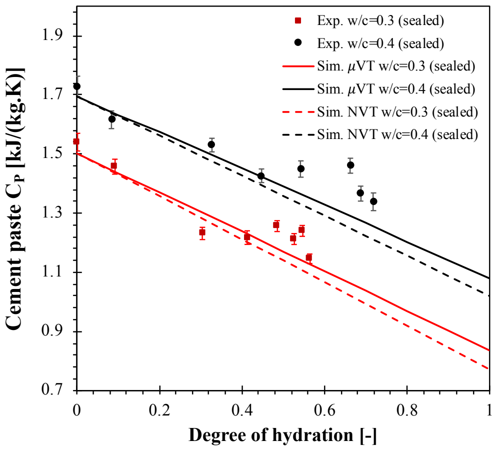

Figure 14: Effective heat capacity C_P of cement pastes with w/c of 0.3 and 0.4: comparison of estimates using input from molecular simulation and the experimental results of Bentz [11]. Solid lines correspond to the case in which results from μVT simulations are used for interlayer confined water in C-S-H (C_P =5.6 kJ/(K.kg)); dashed lines, to the case in which results from NVT simulations are used for interlayer confined water in C-S-H (C_P= 3.9 kJ/(K.kg))

3.3.4. Isosteric heat of adsorption

Figure 15 displays the isosteric heat of adsorption q_{st} as a function of the c-length. For comparison, the bulk experimental and SPC/E water vaporization enthalpy are shown. An isosteric heat of adsorption above the vaporization enthalpy indicates an enthalpic driving force for further hydration, whilst a q_{st} below the vaporization enthalpy indicates an enthalpic driving force for dehydration. The vaporization enthalpy is retrieved for a system with a c-length exceeding approximately 3 nm. Due to water layering in micropores, a damped oscillatory q_{st} profile as a function of the basal spacing, with q_{st} at large basal spacings tending to the vaporization enthalpy, is expected [79]. The oscillations are not very well distinguishable in our results (as is the case of clays [79]), and that may be due to the interference of the roughness of C-S-H layer surfaces on water ordering (as depicted in Figure 4).

As a summary, Table 4 gathers the properties of confined water in C-S-H according to the stable hydration states discussed in Section 3.1.

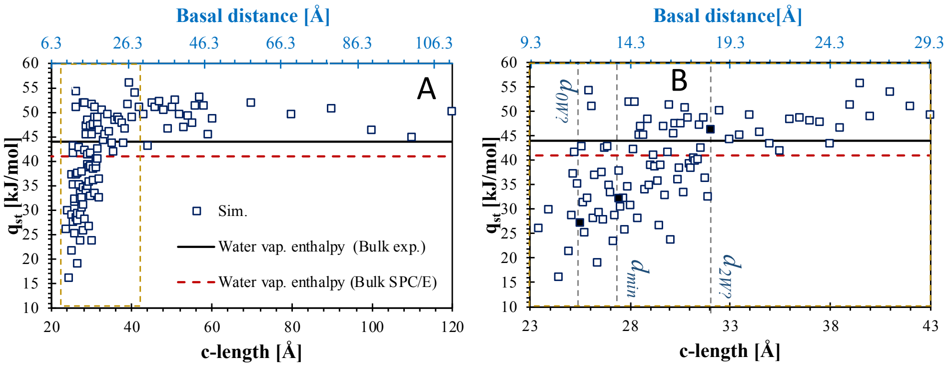

Figure 15: (A) Isosteric heat of adsorption q_{st} as a function of the c-length. Bulk experimental and SPC/E water vaporization enthalpy are shown for reference. (B) shows the details on the 23-43 Å c-length range. The experimental and SPC/E model values of the vaporization enthalpy of bulk water is taken from ref. [69].

4. Discussion: why property changes with confinement?

Changes in the structure of water due to adsorption and confinement are expected to be at the origin of the changes in properties observed in the last section. A direct relation between a structural quantifier and the properties evolution is not simple to be established, though. In addition to the apparent density (Figure 9), which can also be used as a structure quantifier, we compute the pair excess entropy S_2 and the number of hydrogen bonds as detailed in the following.

4.1. Entropy

To quantify the relative order in a molecular system, we use the concept of excess entropy, which has been connected to the structure, thermodynamics, and transport properties of liquid and disordered systems [80], including C-S-H [81]. The pair (first-order) excess entropy S_2 can be computed from the pair

Table 4: Properties of water confined in C-S-H according to the stable basal spacings $d_{0W?}$, d_{min} and $d_{2W?}$. Data from experimental studies from the literature simulations and simulation results of bulk SPC/E water are shown for comparison.

Property		$d_{0W?}$	d_{min}	$d_{2W?}$	(Bulk) Exp.	Bulk SPC/E
ρ	g/cm^3	1.48	1.39	1.27	1.0	0.997 [69]; 0.996 ± 0.006*
K	[GPa]	7.1	8.1	1.8	2.2 [68]	2.4; 3.4 ± 0.4*
β_T	[10^{-11}/Pa]	14.1	12.3	54.9	45.2 [68]	41.4 ± 1.95 [68]; 29.5 ± 2.9*
γ_V	[MPa/K]	0.13	-3.9	4.3	5 **	14.5**; 68.0 ± 4.4*
α_V	[10^{-5}/K]	0.19	-4.8	23.5	20.7; 27.0 [69]	51[69]; 19.6 ± 12.2*
α_x	[10^{-5}/K]	0.01	-4.2	20.1	-	-
α_y	[10^{-5}/K]	-1.19	-1.8	38.4	-	-
α_z	[10^{-5}/K]	1.75	-8.4	11.9	-	-
C_V	[kJ/(K.kg)]	5.6	5.6	5.1	4.18 [72]	4.12349 [73]; 3.88 ± 0.16*
C_P	[kJ/(K.kg)]	5.6	5.6	5.1	4.18 [72]	4.51339 [73]; 3.95 ± 0.14*
q_{st}	[kJ/mol]	27.4	32.3	46.3	43.8 [69]	41; 46.1 [69]; 46.9 ± 2.2*

*This work: GCMC simulations in bulk SPC/E water.

** Computed from α_V and K.

radial function g_{i-j} using [82, 80]:

$$\frac{S_2}{kN} = -\frac{2\pi}{V}\sum_{i,j}\int_0^\infty \left[g_{i-j}(r)\,\ln\, g_{i-j}(r) - g_{i-j} + 1\right] r^2 dr \qquad (27)$$

where N is the total number of particles and x_i is the molecular fraction of particle of type i in the system. This formula enables the computation of the pair-wise contribution $S_{2_{i-j}}$ to the total entropy according to the choice of pairs i, j. In Figure 16(A), we compute the contributions associated with the pore fluid or electrolyte, as a sum of the $S_{2_{i-j}}$ involving all pairs i, j=Ow, Hw, Hh, Oh, and Caw combinations; and of water, ass a sum of the $S_{2_{i-j}}$ involving all combinations of Ow, Hw pairs (in all cases, including self-combinations).

The excess entropies are non-monotonous functions of the c-length. For $c >\approx 5$ nm, the total, water, and electrolyte excess entropies are an increasing function, indicating that adding water to the system only contributes to the increase in its entropy. A (less intuitive) decrease in system excess entropy is observed in c-lengths ranging from 33 to 50 Å. The main contributor to the decrease of entropy in this range is the decrease in water entropy, as shown in the inset of Figure 16(A), which reaches a minimum at a c-length of approximately 4 nm. This c-length corresponds to the point in which the second peak of water oxygens RDFs bifurcates (Figure 8). The analysis of Figure 4 also suggests that from a c-length below 4 nm the effects of the layer surface interactions superpose affecting the structure of the electrolyte, and in particular water, in the entire interlayer pore thickness. For c-lengths of at least 4 nm, a portion of the pore (center) start to be occupied by water with bulk density. The minimum is water entropy profile might be therefore correlated to the pore size in which bulk water starts to exist in C-S-H.

4.2. H-bond statistics

H-bond network statistics inform on the degree of constraints in water, and have been linked to changes in the thermo- mechanical properties of layered silicates [83]. The criteria adopted to define a H-bond are [84]: a distance of donor-acceptor oxygens 2.5< d_{HB} <3.5 Å and angle between O-H and O...O vectors θ_{HB} $\leq$100° (see the inset in Figure 16(B)). The total H-bonds HB are computed as the sum of the contribution of water oxygen HB^{WW}, hydroxide groups HB^{HH}, water oxygen and hydroxide groups HB^{WH}, layer oxygen and water oxygen HB^{LW}, and layer oxygen and hydroxide HB^{LH}:

$$HB = HB^{WW} + HB^{HH} + HB^{WH} + HB^{LW} + HB^{LW} \tag{28}$$

For the H-bonds counted in HB^{LW} and HB^{LH}, the oxygens in the layer function only as an acceptor; in the other cases, the oxygens can be both donor or acceptor.

Figure 16(B) shows the total H-bonds HB and the contributions defined above as a function of the c-length for a few selected points. The HB^{WW} retrieves the value associated with bulk water for $c >\approx 7$ nm. A larger number of H-bonds is observed when one accounts for the contributions of oxygens out of water molecules, and this contribution is more significant the smaller the pore. This result indicates that confined fluids are more constrained in what concerns H-bonds than the bulk system. More constraints can explain the higher bulk modulus (respectively, lower isothermal compressibility) of water in ultra-confined systems observed in the previous sections. In liquid systems, the thermal excitation of the H-bond network is associated with the high heat capacity of water [85]. These observations suggest that liquid systems with more H-bonds could present high heat capacity, in agreement with what was discussed in Section 3.3.3.

4.3. Linear correlations between properties and structural descriptors

Table 5: Linear correlations coefficients R^2 of properties computed by simulations and water content, basal spacing d and structural descriptors (density ρ^*, pair excess entropy S_2, and H-bonds per water molecule). The values in-between the parenthesis corresponds to correlations in for systems with c-length greater or equal to 40Å.

	q_{st}	β_T	K	C_V	C_P	α_V	α_x	α_y	α_z	γ_V
N_w	0.17 (0.17)	0.01 (0.44)	0.15 (0.32)	0.67 (0.66)	0.67 (0.68)	0.09 (0.34)	0.10 (0.32)	0.07 (0.41)	0.11 (0.29)	0.20 (0.00)
d	0.18 (0.17)	0.01 (0.44)	0.15 (0.32)	0.67 (0.66)	0.67 (0.69)	0.10 (0.34)	0.11 (0.32)	0.07 (0.41)	0.11 (0.29)	0.20 (0.00)
ρ^*	0.37 (0.08)	0.28 (0.54)	0.50 (0.41)	0.89 (0.67)	0.85 (0.67)	0.34 (0.31)	0.35 (0.29)	0.35 (0.38)	0.32 (0.25)	0.27 (0.00)
S_2	0.15 (0.22)	0.05 (0.43)	0.28 (0.28)	0.76 (0.58)	0.78 (0.66)	0.07 (0.40)	0.08 (0.37)	0.07 (0.46)	0.07 (0.34)	0.12 (0.01)
S_2 (elec.)	0.21 (0.17)	0.07 (0.51)	0.30 (0.35)	0.83 (0.66)	0.83 (0.71)	0.14 (0.40)	0.14 (0.37)	0.12 (0.46)	0.14 (0.33)	0.18 (0.00)
S_2 (wat.)	0.02 (0.17)	0.11 (0.54)	0.00 (0.38)	0.23 (0.65)	0.25 (0.72)	0.00 (0.42)	0.00 (0.39)	0.01 (0.49)	0.00 (0.35)	0.07 (0.00)
HB	0.37 (0.08)	0.23 (0.63)	0.48 (0.49)	0.89 (0.64)	0.85 (0.69)	0.31 (0.39)	0.32 (0.37)	0.31 (0.47)	0.29 (0.32)	0.28 (0.00)
HB^{WW}	0.27 (0.06)	0.20 (0.44)	0.43 (0.39)	0.93 (0.81)	0.91 (0.71)	0.25 (0.21)	0.26 (0.19)	0.25 (0.27)	0.24 (0.16)	0.21 (0.01)
HB^{HH}	0.26 (0.18)	0.32 (0.71)	0.59 (0.45)	0.75 (0.42)	0.72 (0.59)	0.20 (0.58)	0.20 (0.56)	0.23 (0.65)	0.16 (0.51)	0.10 (0.01)
HB^{WH}	0.37 (0.07)	0.16 (0.53)	0.39 (0.42)	0.83 (0.74)	0.79 (0.70)	0.33 (0.29)	0.34 (0.27)	0.30 (0.36)	0.34 (0.23)	0.39 (0.01)
HB^{LW}	0.32 (0.07)	0.21 (0.55)	0.44 (0.45)	0.92 (0.75)	0.89 (0.72)	0.29 (0.30)	0.30 (0.28)	0.29 (0.37)	0.28 (0.24)	0.26 (0.00)
HB^{LH}	0.23 (0.07)	0.26 (0.48)	0.47 (0.41)	0.76 (0.78)	0.74 (0.71)	0.18 (0.25)	0.18 (0.23)	0.21 (0.31)	0.14 (0.19)	0.09 (0.00)

In Table 5, using the linear R^2 coefficient, we quantify the correlations between the computed properties of confined water and the water content, basal spacing d and structural descriptors such as the density ρ^*, the pair excess entropy S_2, and the number f H-bonds per water molecule. For the heat capacity, only GCMC results were considered. It is important to highlight that correlations with a small linear R^2 may be an indication of parameters that are

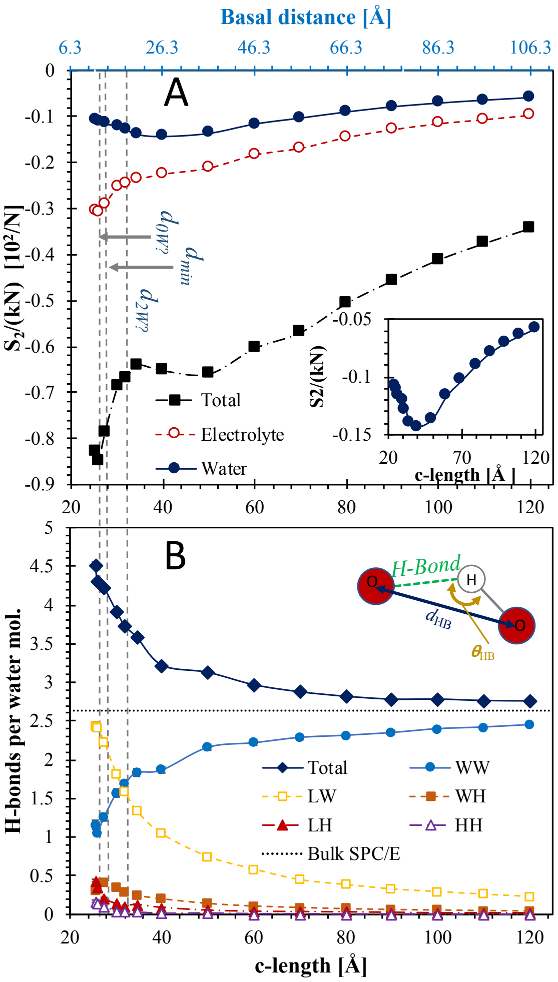

Figure 16: (A) Pair excess entropy S_2 ("electrolyte" refers to the sum of all pairs i,j=Ow, Hw, Hh, Oh, and Caw combinations; "water" refers to the sum of all pairs i,j=Ow, Hw combinations), and (B) H-bonds per water molecule (and the contributions of water-water HB^{WW}, hydroxide-hydroxide HB^{HH}, water-hydroxide HB^{WH}, layer-hydroxide HB^{LW}, and layer-water HB^{LW} bonds) as a function of the c-length. We selected a few points covering the whole range of c-length in figures.

correlated but not following a linear relation. The same points as in Figure 16 have been used to compute the correlations. See the Supporting Information for the graphics with each property plotted against each structural descriptor.

The most significant linear correlations are observed between the descriptors and the heat capacities. Heat capacity displays a good correlation with the total and electrolyte entropy. This observation is in agreement with experimental considerations showing that the heat capacity is linearly correlated to the entropy for hydrated mineral calcium silicates [86]. The heat capacity also shows a significant linear correlation with the total, water, and layer-water H-bonds number as well as the apparent density.

The isosteric heat of adsorption and the coefficients of thermal expansion exhibit a small linear association with the apparent density, total and water-hydroxide H-bonds. No significant linear correlations are observed between the coefficients of thermal pressure and the descriptors considered. Structural changes of adsorbed water have been evoked to explain the changes in the coefficient of thermal expansion of water confined in porous silica [87]. The structure descriptors used here might not capture the relevant structural changes. Also, the large noise associated with the results of the computed coefficients of thermal expansion impairs the computation of a precise correlation.

The number of H-bonds per water molecule shows a small linear correlation with the bulk modulus. No significant linear correlation with the isothermal compressibility is observed except for the hydroxide H-bonds. These observations may suggest that the nature of the H-bond (strong or weak [84]) may play a crucial role. H-bonds involving OH groups outside water molecules have been reported as presenting higher energy [88] than the one involving only water. Also confined water itself may present H-bonds with higher rigidity under confinement [89]. Further studies including the energetics of H-bonds may shed light on the influence of the nature of H-bonds on constraining confined fluids.

5. Conclusion

In this work, we analyzed how confinement affects the thermomechanical properties of water in C-S-H using molecular simulations. For the first time, fluctuations formula in the grand canonical ensemble were used to compute directly the properties of confined water in C-S-H. The results provided here can be used as input in multiscale modeling of thermomechanical processes in cement-based materials.

Molecular simulation under drained conditions shows that the thermomechanical properties of water confined in C-S-H are dependent on pore size, following the example of transport and electromagnetic properties [9, 30, 4, 2]. For the bulk modulus, isothermal compressibility, heat capacities, and coefficients of thermal expansion and thermal pressure the bulk values are retrieved for basal spacings as small as 16.3-26.3 Å (i.e. c-lengths of approximately 3-4 nm).

Property change of fluids under confinement has been associated with fluid structural changes in the literature. We correlated the computed properties with structure description such as the apparent density, the excess entropy, and H-bonds statistics. Good linear correlations were obtained for the heat capacities. Further studies are needed to explain the origins of property change due to confinement in mechanical properties, isosteric heat of adsorption, and thermal expansion coefficients. Other structural descriptors or plus precise H-bonds statistics may be helpful.

Similar strategies can be deployed to understand the effect of confinement in other layered materials in cement systems such as crystalline ASR products or AFms [75, 90]. Multiscale modeling of cement-based materials can improve its precision by accounting for the pore-size dependence of confined fluids. One should pay particular attention to the pore sizes associated with a stable equilibrium.

Acknowledgement

The financial support of the French National Research Agency (ANR) through the project THEDESCO (ANR-19-CE22-0004-01) is gratefully acknowledged.

References

References

[1] A. Botan, B. Rotenberg, V. Marry, P. Turq, B. Noetinger, Hydrodynamics in Clay Nanopores, The Journal of Physical Chemistry C 115 (32) (2011) 16109–16115.

[2] M. Youssef, R. J.-M. Pellenq, B. Yildiz, Glassy Nature of Water in an Ultraconfining Disordered Material: The Case of CalciumSilicateHydrate, Journal of the American Chemical Society 133 (8) (2011) 2499–2510.

[3] R. Bergman, J. Swenson, Dynamics of supercooled water in confined geometry, Nature 403 (6767) (2000) 283.

[4] S. Masoumi, S. Zare, H. Valipour, M. J. Abdolhosseini Qomi, Effective Interactions between Calcium-Silicate-Hydrate Nanolayers, The Journal of Physical Chemistry C 123 (8) (2019) 4755–4766.

[5] F. M. Etzler, P. J. White, The heat capacity of water in silica pores, Journal of Colloid and Interface Science 120 (1) (1987) 94–99.

[6] T. Honorio, T. Lemaire, D. D. Tommaso, S. Naili, Molecular modelling of the heat capacity and anisotropic thermal expansion of nanoporous hydroxyapatite, Materialia (2019) 100251.

[7] T. Honorio, L. Brochard, M. Vandamme, Effective stresses and estimations of the apparent Biot coefficient in stacked clay layers, Géotechnique Letters 8 (2) (2018) 97–101.

[8] I. Brovchenko, A. Oleinikova, Interfacial and Confined Water, Elsevier, 2008.

[9] H. Manzano, S. Moeini, F. Marinelli, A. C. T. van Duin, F.-J. Ulm, R. J.-M. Pellenq, Confined Water Dissociation in Microporous Defective Silicates: Mechanism, Dipole Distribution, and Impact on Substrate Properties, Journal of the American Chemical Society 134 (4) (2012) 2208–2215.

[10] M. J. A. Qomi, L. Brochard, T. Honorio, I. Maruyama, M. Vandamme, Advances in Atomistic Modeling and Understanding of Drying Shrinkage in Cementitious Materials, Cement and Concrete Research (submitted).

[11] D. P. Bentz, Transient plane source measurements of the thermal properties of hydrating cement pastes 40 (10) 1073–1080. `doi:10.1617/s11527-006-9206-9`.

[12] M. J. A. Qomi, F.-J. Ulm, R. J.-M. Pellenq, Physical Origins of Thermal Properties of Cement Paste, Physical Review Applied 3 (6) (2015) 064010.

[13] P. F. Low, Nature and properties of water in montmorillonite-water systems 43 (4) 651–658. `doi:https://doi.org/10.2136/sssaj1979.03615995004300040005x`.

[14] F. M. Etzler, Enhancement of hydrogen bonding in vicinal water; heat capacity of water and deuterium oxide in silica pores 4 (4) 878–883. `doi:10.1021/la00082a017`.

[15] A. Nolasco, E. Julien, J. Besombes-Vailhe, Partial molar heat capacity of adsorbed water on an ion-exchanger 92 341–344. `doi:10.1016/0040-6031(85)85886-X`.

[16] F. M. Etzler, A statistical thermodynamic model for water near solid interfaces 92 (1) 43–56. `doi:10.1016/0021-9797(83)90115-7`.

[17] F. M. Etzler, J. J. Conners, Structural transitions in vicinal water: pore size and temperature dependence of the heat capacity of water in small pores, Langmuir 7 (10) (1991) 2293–2297.

[18] H. Manzano, E. Masoero, I. Lopez-Arbeloa, H. M. Jennings, Shear deformations in calcium silicate hydrates 9 (30) 7333. `doi:10.1039/c3sm50442e`.

[19] J. L. Oliphant, P. F. Low, The isothermal compressibility of water mixed with na-saturated montmorillonite 95 (1) 45–50. `doi:10.1016/0021-9797(83)90070-X`.

[20] P. A. Bonnaud, Q. Ji, B. Coasne, R. J.-M. Pellenq, K. J. Van Vliet, Thermodynamics of Water Confined in Porous Calcium-Silicate-Hydrates, Langmuir 28 (31) (2012) 11422–11432.

[21] L. Brochard, T. Honrio, Revisiting thermo-poro-mechanics under adsorption: Formulation without assuming gibbs-duhem equation 152 103296. `doi:10.1016/j.ijengsci.2020.103296`.

[22] L. Brochard, T. Honrio, Thermo-poro-mechanics under adsorption applied to the anomalous thermal pressurization of water in undrained clays`doi:10.1007/s11440-021-01188-8`.

[23] A. Kunhi Mohamed, S. C. Parker, P. Bowen, S. Galmarini, An atomistic building block description of C-S-H - Towards a realistic C-S-H model, Cement and Concrete Research 107 (2018) 221–235.

[24] I. G. Richardson, Tobermorite/jennite- and tobermorite/calcium hydroxide-based models for the structure of C-S-H: applicability to hardened pastes of tricalcium silicate, beta-dicalcium silicate, Portland cement, and blends of Portland cement with blast-furnace slag, metakaolin, or silica fume, Cement and Concrete Research 34 (9) (2004) 1733–1777.

[25] A. J. Allen, J. J. Thomas, H. M. Jennings, Composition and density of nanoscale calcium–silicate–hydrate in cement, Nature Materials 6 (4) (2007) 311–316.

[26] A. C. A. Muller, K. L. Scrivener, A. M. Gajewicz, P. J. McDonald, Densification of C–S–H Measured by 1H NMR Relaxometry, The Journal of Physical Chemistry C 117 (1) (2012) 403–412.

[27] R. T. Cygan, J.-J. Liang, A. G. Kalinichev, Molecular Models of Hydroxide, Oxyhydroxide, and Clay Phases and the Development of a General Force Field, The Journal of Physical Chemistry B 108 (4) (2004) 1255–1266.

[28] H. J. C. Berendsen, J. R. Grigera, T. P. Straatsma, The missing term in effective pair potentials, The Journal of Physical Chemistry 91 (24) (1987) 6269–6271.

[29] T. Honorio, L. Brochard, M. Vandamme, Hydration Phase Diagram of Clay Particles from Molecular Simulations, Langmuir 33 (44) (2017) 12766–12776.

[30] T. Honorio, Monte Carlo Molecular Modeling of Temperature and Pressure Effects on the Interactions between Crystalline Calcium Silicate Hydrate Layers, Langmuir 35 (11) (2019) 3907–3916.

[31] L. Brochard, T. Honrio, M. Vandamme, M. Bornert, M. Peigney, Nanoscale origin of the thermo-mechanical behavior of clays 12 (6) 1261–1279. `doi:10.1007/s11440-017-0596-3`.

[32] M. P. Allen, D. J. Tildesley, Computer Simulation of Liquids, Oxford University Press, New York, 1989.

[33] B. Z. Shang, Multiscale simulations: From enzyme kinetics to fluctuating hydrodynamics (2013) 167.

[34] P. Schofield, Wavelength-dependent fluctuations in classical fluids: I. the long wavelength limit 88 (1) 149–170. `doi:10.1088/0370-1328/88/1/318`.

[35] S. Poyet, S. Charles, Temperature dependence of the sorption isotherms of cement-based materials: Heat of sorption and clausiusclapeyron formula 39 (11) (2009) 1060–1067. `doi:10.1016/j.cemconres.2009.07.018`.

[36] D. Nicholson, Computer simulation and the statistical mechanics of adsorption, Academic Press, 1982.

[37] P. A. Bonnaud, H. Manzano, R. Miura, A. Suzuki, N. Miyamoto, N. Hatakeyama, A. Miyamoto, Temperature Dependence of Nanoconfined Water Properties: Application to Cementitious Materials, The Journal of Physical Chemistry C.

[38] Y. Yang, R. Qiao, Y. Wang, S. Sun, Swelling pressure of montmorillonite with multiple water layers at elevated temperatures and water pressures: A molecular dynamics study, Applied Clay Science (2020) 105924.

[39] C. Plassard, E. Lesniewska, I. Pochard, A. Nonat, Nanoscale experimental investigation of particle interactions at the origin of the cohesion of cement 21 (16) 7263–7270. `doi:10.1021/la050440+`.

[40] P. A. Bonnaud, C. Labbez, R. Miura, A. Suzuki, N. Miyamoto, N. Hatakeyama, A. Miyamoto, K. J. V. Vliet, Interaction grand potential between calcium–silicate–hydrate nanoparticles at the molecular level, Nanoscale 8 (7) (2016) 4160–4172.

[41] R. J. M. Pellenq, N. Lequeux, H. van Damme, Engineering the bonding scheme in C–S–H: The iono-covalent framework, Cement and Concrete Research 38 (2) (2008) 159–174.

[42] S. Masoumi, H. Valipour, M. J. Abdolhosseini Qomi, Intermolecular Forces between Nanolayers of Crystalline Calcium-Silicate-Hydrates in Aqueous Medium, The Journal of Physical Chemistry C 121 (10) (2017) 5565–5572.

[43] S. Brunauer, D. L. Kantro, C. H. Weise, The Surface Energy of Tobermorite, Canadian Journal of Chemistry 37 (4) (1959) 714–724.

[44] S. Brunauer, Surfaces of solids, Pure and Applied Chemistry 10 (4) (1965) 293–308.

[45] J. E. Oh, S. M. Clark, P. J. M. Monteiro, Does the Al substitution in C–S–H(I) change its mechanical property?, Cement and Concrete Research 41 (1) (2011) 102–106.

[46] J. E. Oh, S. M. Clark, H.-R. Wenk, P. J. Monteiro, Experimental determination of bulk modulus of 14 å tobermorite using high pressure synchrotron X-ray diffraction, Cement and Concrete Research 42 (2) (2012) 397–403.

[47] S. Grangeon, A. Fernandez-Martinez, A. Baronnet, N. Marty, A. Poulain, E. Elkaïm, C. Roosz, S. Gaboreau, P. Henocq, F. Claret, Quantitative X-ray pair distribution function analysis of nanocrystalline calcium silicate hydrates: a contribution to the understanding of cement chemistry, Journal of Applied Crystallography 50 (1) (2017) 14–21.

[48] Y. Aierken, H. Sahin, F. Iyikanat, S. Horzum, A. Suslu, B. Chen, R. T. Senger, S. Tongay, F. M. Peeters, Portlandite crystal: Bulk, bilayer, and monolayer structures, Physical Review B 91 (24) (2015) 245413.

[49] A. L. Thorneywork, R. Roth, D. G. A. L. Aarts, R. P. A. Dullens, Communication: Radial distribution functions in a two-dimensional binary colloidal hard sphere system, The Journal of Chemical Physics 140 (16) (2014) 161106.

[50] S. SoyerUzun, S. R. Chae, C. J. Benmore, H.-R. Wenk, P. J. M. Monteiro, Compositional Evolution of Calcium Silicate Hydrate (C–S–H) Structures by Total X-Ray Scattering, Journal of the American Ceramic Society 95 (2) (2012) 793–798.

[51] H. E. Fischer, A. C. Barnes, P. S. Salmon, Neutron and x-ray diffraction studies of liquids and glasses 69 (1) 233–299. `doi:10.1088/0034-4885/69/1/R05`.

[52] C. Meral, C. J. Benmore, P. J. M. Monteiro, The study of disorder and nanocrystallinity in csh, supplementary cementitious materials and geopolymers using pair distribution function analysis 41 (7) 696–710. `doi:10.1016/j.cemconres.2011.03.027`.

[53] R. J.-M. Pellenq, A. Kushima, R. Shahsavari, K. J. V. Vliet, M. J. Buehler, S. Yip, F.-J. Ulm, A realistic molecular model of cement hydrates, Proceedings of the National Academy of Sciences 106 (38) (2009) 16102–16107.

[54] J. Janik, W. Kurdowski, R. Podsiadły, J. Samseth, Fractal Structure of

C-S-H and Tobermorite Phases, Acta Physica Polonica A 100 (4) (2001) 529–537.

[55] X. Cong, R. J. Kirkpatrick, Effects of the temperature and relative humidity on the structure of CSH gel, Cement and Concrete Research 25 (6) (1995) 1237–1245.

[56] S. I. Martin, Synthesis of tobermorite: A cement phase expected under repository conditions, Tech. Rep. UCRL-JC-119131; CONF-950570-2, Lawrence Livermore National Lab., CA (United States) (Nov. 1994).

[57] I. G. Richardson, Model structures for C-(A)-S-H(I), Acta Crystallographica Section B: Structural Science, Crystal Engineering and Materials 70 (6) (2014) 903–923.

[58] E. Gartner, I. Maruyama, J. Chen, A new model for the C-S-H phase formed during the hydration of Portland cements, Cement and Concrete Research 97 (2017) 95–106.

[59] A. Morshedifard, S. Masoumi, M. J. A. Qomi, Nanoscale origins of creep in calcium silicate hydrates, Nature Communications 9 (1) (2018) 1785.

[60] A. C. A. Muller, K. L. Scrivener, A. M. Gajewicz, P. J. McDonald, Use of bench-top NMR to measure the density, composition and desorption isotherm of C–S–H in cement paste, Microporous and Mesoporous Materials 178 (2013) 99–103.

[61] H. F. W. Taylor, Cement chemistry, 2nd Edition, T. Telford, London, 1997.

[62] G. L. Kalousek, A. F. Prebus, Crystal Chemistry of Hydrous calcium Silicates: III, Morphology and Other Properties of Tobermorite and Related Phases, Journal of the American Ceramic Society 41 (4) (1958) 124–132.

[63] E. L'Hôpital, B. Lothenbach, D. A. Kulik, K. Scrivener, Influence of calcium to silica ratio on aluminium uptake in calcium silicate hydrate, Cement and Concrete Research 85 (2016) 111–121.

[64] K. Garbev, G. Beuchle, M. Bornefeld, L. Black, P. Stemmermann, Cell Dimensions and Composition of Nanocrystalline Calcium Silicate Hydrate Solid Solutions. Part 1: Synchrotron-Based X-Ray Diffraction, Journal of the American Ceramic Society 91 (9) (2008) 3005–3014.

[65] D. Sugiyama, Chemical alteration of calcium silicate hydrate (C–S–H) in sodium chloride solution, Cement and Concrete Research 38 (11) (2008) 1270–1275.

[66] G. Geng, R. J. Myers, M. J. A. Qomi, P. J. M. Monteiro, Densification of the interlayer spacing governs the nanomechanical properties of calcium-silicate-hydrate, Scientific Reports 7 (1) (2017) 10986.

[67] M. J. A. Qomi, K. J. Krakowiak, M. Bauchy, K. L. Stewart, R. Shahsavari, D. Jagannathan, D. B. Brommer, A. Baronnet, M. J. Buehler, S. Yip, F.-J. Ulm, K. J. V. Vliet, R. J.-M. Pellenq, Combinatorial molecular optimization of cement hydrates, Nature Communications 5 (2014) 4960.

[68] K. A. Motakabbir, M. Berkowitz, Isothermal compressibility of SPC/E water, The Journal of Physical Chemistry 94 (21) (1990) 8359–8362.

[69] R. Fuentes-Azcatl, N. Mendoza, J. Alejandre, Improved SPC force field of water based on the dielectric constant, Physica A: Statistical Mechanics and its Applications 420 (2015) 116–123.

[70] E. Keszei, Chemical Thermodynamics, Springer Berlin Heidelberg. `doi:10.1007/978-3-642-19864-9`.
URL `http://link.springer.com/10.1007/978-3-642-19864-9`

[71] P. G. Debenedetti, Supercooled and glassy water 15 (45) R1669, publisher: IOP Publishing. `doi:10.1088/0953-8984/15/45/R01`.
URL `https://iopscience.iop.org/article/10.1088/0953-8984/15/45/R01/meta`

[72] W. M. Haynes, CRC Handbook of Chemistry and Physics, 95th Edition, CRC Press, 2014.

[73] Y. Mao, Y. Zhang, Thermal conductivity, shear viscosity and specific heat of rigid water models, Chemical Physics Letters 542 (2012) 37–41.

[74] P. Simonnin, B. Noetinger, C. Nieto-Draghi, V. Marry, B. Rotenberg, Diffusion under confinement: Hydrodynamic finite-size effects in simulation 13 (6) 2881–2889. `doi:10.1021/acs.jctc.7b00342`.

[75] T. Honorio, O. M. Chemgne Tamouya, Z. Shi, A. Bourdot, Intermolecular interactions of nanocrystalline alkali-silica reaction products under sorption, Cement and Concrete Research 136 (2020) 106155.

[76] T. Honorio, B. Bary, F. Benboudjema, Thermal properties of cement-based materials: Multiscale estimations at early-age, Cement and Concrete Composites 87 (2018) 205–219. `doi:10.1016/j.cemconcomp.2018.01.003`.
URL `http://www.sciencedirect.com/science/article/pii/S0958946516305200`

[77] M. Knigsberger, C. Hellmich, B. Pichler, Densification of C-S-H is mainly driven by available precipitation space, as quantified through an analytical cement hydration model based on NMR data, Cement and Concrete Research 88 (2016) 170–183. `doi:10.1016/j.cemconres.2016.04.006`.
URL `http://www.sciencedirect.com/science/article/pii/S0008884616303374`

[78] T. Matschei, B. Lothenbach, F. P. Glasser, Thermodynamic properties of Portland cement hydrates in the system CaOAl2O3SiO2CaSO4CaCO3H2O, Cement and Concrete Research 37 (10) (2007) 1379–1410. `doi:10.1016/j.cemconres.2007.06.002`.
URL `http://www.sciencedirect.com/science/article/pii/S0008884607001299`

[79] D. E. Smith, Molecular computer simulations of the swelling properties and interlayer structure of cesium montmorillonite 14 (20) 5959–5967. `doi:10.1021/la980015z`.
URL `https://doi.org/10.1021/la980015z`

[80] F. Pacaud, M. Micoulaut, Thermodynamic precursors, liquid-liquid transitions, dynamic and topological anomalies in densified liquid germania, The Journal of Chemical Physics 143 (6) (2015) 064502.

[81] M. Bauchy, M. J. A. Qomi, F.-J. Ulm, R. J.-M. Pellenq, Order and disorder in calcium–silicate–hydrate, The Journal of Chemical Physics 140 (21) (2014) 214503.

[82] A. Baranyai, D. J. Evans, Direct entropy calculation from computer simulation of liquids, Physical Review A 40 (7) (1989) 3817–3822.

[83] T. Honorio, O. M. Chemgne Tamouya, Z. Shi, Specific ion effects control the thermoelastic behavior of nanolayered materials: the case of crystalline alkali-silica reaction products, Physical Chemistry Chemical Physics.

[84] Y. Marcus, Effect of Ions on the Structure of Water: Structure Making and Breaking, Chemical Reviews 109 (3) (2009) 1346–1370.

[85] S. V. Lishchuk, N. P. Malomuzh, P. V. Makhlaichuk, Contribution of h-bond vibrations to heat capacity of water 375 (27) 2656–2660. `doi:10.1016/j.physleta.2011.05.049`.
URL `https://www.sciencedirect.com/science/article/pii/S037596011100658X`

[86] L. Glasser, The effective volumes of waters of crystallization & the thermodynamics of cementitious materials 3 100004. `doi:10.1016/j.cement.2021.100004`.

[87] S. Xu, G. W. Scherer, T. S. Mahadevan, S. H. Garofalini, Thermal Expansion of Confined Water, Langmuir 25 (9) (2009) 5076–5083.

[88] M. Chen, B. Coasne, R. Guyer, D. Derome, J. Carmeliet, Role of hydrogen bonding in hysteresis observed in sorption-induced swelling of soft nanoporous polymers, Nature Communications 9 (1) (2018) 3507.

[89] D. Di Tommaso, M. Prakash, T. Lemaire, M. Lewerenz, N. H. de Leeuw, S. Naili, Molecular Dynamics Simulations of Hydroxyapatite Nanopores in Contact with Electrolyte Solutions: The Effect of Nanoconfinement and Solvated Ions on the Surface Reactivity and the Structural, Dynamical, and Vibrational Properties of Water, Crystals 7 (2) (2017) 57.

[90] T. Honorio, P. Guerra, A. Bourdot, Molecular simulation of the structure and elastic properties of ettringite and monosulfoaluminate, Cement and Concrete Research 135 (2020) 106126.

Declaration of interests

The authors declare that they have no known competing financial interests or personal relationships that could have appeared to influence the work reported in this paper.